Institute of Experimental Physics

Prof. Dr. Kay-E. Gottschalk



A Mechanobiosensor for Lung Cells

Dissertation to obtain the degree Dr.rer.nat. of the Faculty of Natural Sciences of Ulm University.

Susan Tavakoli

Mashhad

2021

Dean of the faculty:

Prof. Dr. Thorsten Bernhardt

Institute of Surface Chemistry and Catalysis, Ulm University, Ulm, Germany

First reviewer:

Prof. Dr. Kay-E Gottschalk

Institute of Experimental Physics, Ulm University, Ulm, Germany

Second reviewer:

Prof. Dr. Manfred Frick

Institute of General Physiology, Ulm University, Ulm, Germany

Date doctorate awarded: 03.06.2022

Contents

1 Introduction **1**

1.1 Mechanical forces in biological system 1

1.1.1 Alveolar cells and cyclic stretch 2

1.2 Traction force microscopy 4

1.2.1 Cell traction forces 4

1.2.2 Measurement methods 4

2 Methodology **9**

2.1 Experiment set-up and substrates 9

2.1.1 Materials 9

2.1.2 Substrate preparation 10

2.1.3 Stretcher device 13

2.1.4 Cell culture 14

2.2 Experiment methods 14

2.2.1 CTF measurement without external stress 14

2.2.2 CTF measurement under uniaxial external strain 15

2.2.3 CTF measurement under fluid-induced shear stress 16

2.3 Data processing 17

3 Results **21**

3.1 Membrane structure 21
3.2 Image analysis 29
3.3 Cell traction force measurements 34
3.3.1 CTFs of unstretched cells 34
3.3.2 CTFs of uniaxially stretched cells 36
3.3.3 CTFs of cells under fluidic shear stress 43

4 Discussion **45**
4.1 Methods overview 45
4.2 Experiments results 46
4.2.1 Traction forces of unstretched cells 46
4.2.2 Traction forces of stretched cells 47
4.2.3 Traction forces of cells under fluidic shear stress 50
4.3 Conclusion 51

5 Summary **53**

A Gel thickness calculation **67**

B Additional codes **69**

List of abbreviations

ATI	alveolar type I epithelial cell
ATII	alveolar type II epithelial cell
ECM	extracellular matrix
CTF	cell traction force
TFM	traction force microscopy
PDMS	polydimethylsiloxane
FTTC	fourier transform traction cytometry
hAELVi^{wt}	human alveolar epithelial lentivirus immortalized cell (wild type)
hAELVi$^{cav-/-}$	caveolin-1 knockout ATI cell

Chapter 1

Introduction

1.1 Mechanical forces in biological system

Mechanotransduction is considered to be the mechanism by which cells convert mechanical stimulus into biochemical reactions. Cells in the human body are experiencing different kinds of mechanical forces depending on the tissue type and their functionality like shear flow in vascular endothelium, compression in bone, stretch in muscle and alveolar cells, etc. It is proved that cells are capable of sensing these forces and they respond by molecular pathways that play important role in regulating the developmental, physiological, and pathological processes at both cellular and tissue levels (Vogel & Sheetz, 2006; Discher et al., 2005). Cell differentiation (Engler et al., 2006), migration (Lo et al., 2000), and death (Chiu et al., 2007) based on matrix elasticity, change of morphology under shear stress(Li et al., 2005), stretch-induced cytoskeleton reorganization and change of stiffness (Gavara et al., 2008; Trepat et al., 2007), and cell death after tension reduction (Grinnell et al., 1999) are few examples of these modulating responses.

Although the exact mechanisms of mechanosensing and initiation of different pathways are not completely known, many molecular structures are shown to have mechanosensing ability. Transmembrane ion channels are one of the well-known structures that are involved in sensing and signaling mechanical forces (Martinac, 2004). They can be

activated or inactivated not by the hydrostatic pressure but by the mechanical tension along the membrane. Another group widely investigated for their mechanosensing role are cytoskeleton (N. Wang et al., 1993) and actin filaments (Hayakawa et al., 2012) and various compounds in the focal adhesion structure like integrin (Geiger et al., 2009; Shyy & Chien, 2002) and other cytoskeleton associated proteins (Yonemura et al., 2010; Puchner et al., 2008) and myosin motor (Laakso et al., 2008; Kee & Robinson, 2008).

1.1.1 Alveolar cells and cyclic stretch

Lung cells are constantly undergoing mechanical stretch during breathing. In the mammalian lung, the alveolus, the endpoint of the respiratory tree where the gas exchange takes place, is a thin epithelium made of alveolar epithelial type I (ATI) and type II (ATII) cells. Together with capillary endothelial cells and a thin basement membrane which is made of extracellular matrix (ECM) proteins mainly collagen and elastin (Suki et al., 2005), alveolar epithelium constructs the air-blood barrier. ATI cells are squamous cells covering more than 95% of the alveolar surface as the thin layer for gas exchange. Cuboidal ATII cells despite their lower alveolar surface coverage are higher in number and they are responsible for the secretion of pulmonary surfactant; a lipoprotein-like substance that prevents the unstable structure of alveoli from collapsing by reducing the surface tension (Figure 1.1).

Stretch in the lung also plays a significant role in regulating lung function and signaling. Studies have already shown the role of stretching in surfactant secretion (Edwards, 2001), permeability (Cohen et al., 2008), lung development (Torday et al., 1998; Liu & Post, 2000), tissue remodeling (Lambert et al., 1992), proliferation (Liu et al., 1992) and ATII cell differentiation (Sanchez-Esteban et al., 2001; Foster et al., 2010). These stretch-induced processes also require sensing, to begin with. One of the candidates for stretch sensing in alveolar cells are caveolae.

Caveolae are invaginations in the plasma membrane of endothelial and epithelial cells (Figure 1.2). It is well established that caveolae existence is associated with caveolin-1 protein (Rothberg et al., 1992). ATI cells are among the cell types that express high levels of caveolin-1 and cells with caveolin-1 deficiency lack caveolae (Frank

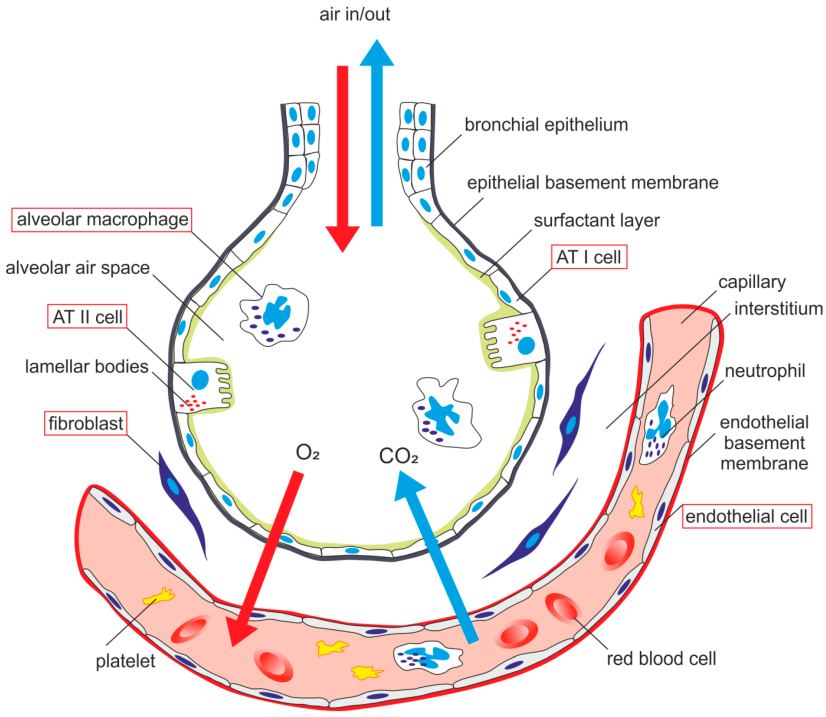

Figure 1.1: Schematic of an alveolus at the air-blood barrier. Squamous ATI cells provide the gas exchanging thin layer and cuboidal ATII cells secret surfactant through the release of lamellar bodies, reducing the surface tension at the air-blood barrier. Reused with permission from Nova et al. (2019) licensed under CC BY 4.0 https://creativecommons.org/licenses/by/4.0/.

et al., 2003). Many dysfunctions have been observed in caveolin-1 deficient mice, indicating the role of these structures in signaling and regulating pathways of the lung cells (Drab et al., 2001). This led to the belief that caveolae participate in mechanosensing (Park et al., 2000; Boyd et al., 2003). Furthermore, caveolae can reduce the mechanical tension on the plasma membrane by expanding during the stretch (Sinha et al., 2011) and activating ion channels in caveolae, and initiating a pathway leading to surfactant secretion (Diem et al., 2020). Caveolae are also associated with stress fibers, which suggests that they participate in actin-controlled pathways in response to mechanical forces (Echarri & Del Pozo, 2015). Studies have shown that in alveolar cells stiffness increased with stretch (Trepat et al., 2004) and that in the absence of caveolae, caveolin-1 knockout cardiac cells are stiffer than the normal cells (Grivas et al., 2020).

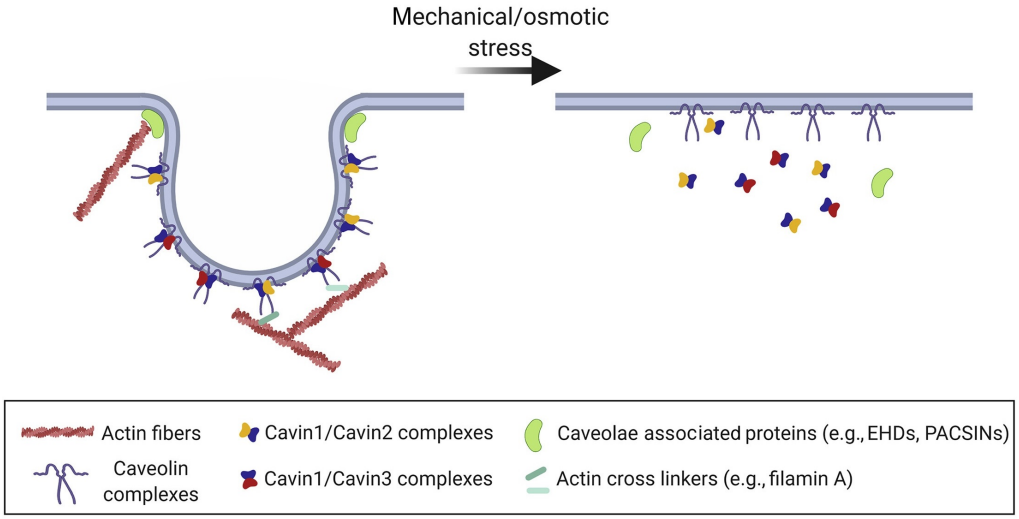

Figure 1.2: Simplified structure of caveolae and their flattening with stretch. They are associated with stress fibers, a major regulator of membrane tension and cell shape. Reused with permission from Rausch & Hansen (2020) licensed under CC BY 4.0 https://creativecommons.org/licenses/by/4.0/.

1.2 Traction force microscopy

1.2.1 Cell traction forces

Cell traction forces (CTFs) are tensile forces generated inside the non-muscle (Figure 1.3) cells by the cytoskeleton and transmitted through focal adhesion to the extracellular matrix or the underlying substrate (N. Balaban et al., 2001). These forces are also vital for many cells functions such as cell migration or wound healing (J. H.-C. Wang & Lin, 2007), and they are also responsive to external mechanical cues like increasing due to substrate stiffness and stretching (Han et al., 2012; N. Wang et al., 1993). Therefore, it is critical to establish methods to quantify CTFs for a better understanding of cell mechanobiology.

1.2.2 Measurement methods

Traction forces are not directly measurable but rather can be calculated by monitoring cell dynamics with their surrounding environment. Throughout the years there have

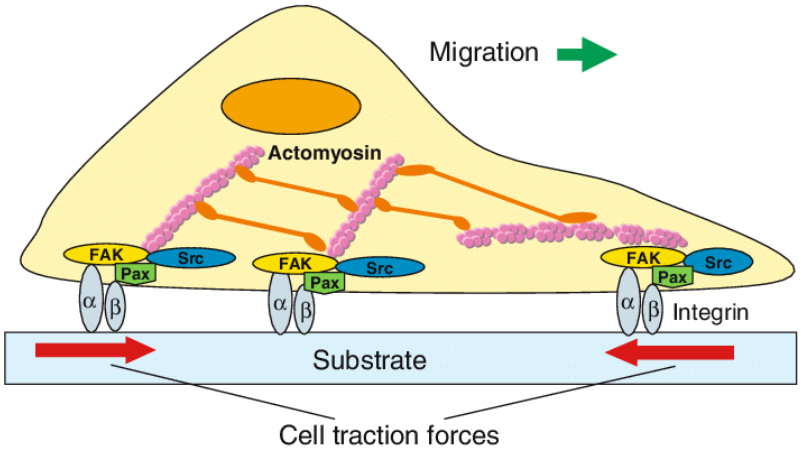

Figure 1.3: Contractile forces exerted by cytoskeleton through focal adhesion on the underlying substrate. From "Cell traction force and measurement methods," by J. H-C. Wang and J-S Lin, 2007, Biomechanics and modeling in mechanobiology, 6, p. 361. Copyright 2007 by Springer Nature. Reprinted with permission.

been several methods developed to measure cell forces (Schwarz & Soiné, 2015). These techniques are referred to as Traction Force Microscopy (TFM). In principle, the dynamic between the cell and its environment is described by Hooke's Law in a linear spring model (Figure 1.4a):

$$F = kx$$

where the force F is the product of the constant factor of spring k, which is experimentally measurable, and the strain x that has to be measured in reference to a relaxation state of the spring (Landau & Lifshitz, 1984). Though being resulted from the applied force, x is the quantity from which this un-measurable force F can be calculated and since the forces created by cells are not discrete like a one-dimensional spring model, it is the tensorial version of Hooke's law that applies and the forces are described as stresses created by a cell on its underlying surface resulting in the creation of a strain field. To provide such a strain field the petri dish or glass is replaced with an elastic medium, soft enough to be deformed by cell forces.

The most commonly used method is to use an elastic film made from polymers gels such as polyacrylamide (PAA) (Y.-L. Wang & Pelham, 1998; Sabass et al., 2008) and polydimethylsiloxane (PDMS) (N. Q. Balaban et al., 2001; Style et al., 2014; Goffin et al., 2006) which their bio-compatibility along with their isotropic and linearly

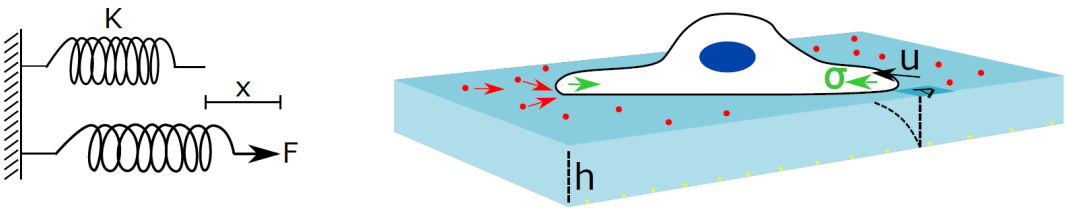

(a) (b)

Figure 1.4: (a) Spring model describing the Hooke's law, (b) Schematic of traction force microscopy. Traction forces are described as stresses $\sigma = F/A$ in Pa. Traction stress σ over the given area A results in displacement u on the surface which means the fluorescent markers near to the area will be displaced accordingly, at the same time the bottom of the film is considered to be fixed on a rigid base. By collecting the displacement of all the fluorescent markers one can compute the displacement field.

elastic properties make them favorite candidates for TFM techniques. To quantify the deformation, fluorescent markers are usually embedded into the body of the elastic film (Maskarinec et al., 2009) or on its surface (Style et al., 2014) the displacement of which will result in the creation of a displacement field (Figure 1.4b). For an isotropic linearly elastic body we have:

$$\sigma = \frac{E}{1-\nu}\left(\frac{1}{2}\left(\nabla\vec{u} + \nabla\vec{u}^{T}\right) + \frac{\nu\nabla\cdot\vec{u}}{1-2\nu}I\right) \tag{1.1}$$

where $\vec{\sigma}$ is the stress, $\vec{u}$ is the displacement, I is the identity tensor, and ν is Poisson's ratio Landau & Lifshitz (1982). In an equilibrium condition for a typical TFM medium $\nabla\cdot\sigma = 0$ which transforms eq. (1.1) into:

$$(1-2\nu)\nabla^2\vec{u} + \vec{\nabla}(\vec{\nabla}\cdot\vec{u}) = 0 \tag{1.2}$$

In general, the solution depends on the boundary conditions of the substrate. For a two-dimensional medium, cell forces are considered tangential since the adherent cells are almost flat. In the case of linear elasticity, the solution is found by using Green's function - the solution for the external point force, while for a non-linear elasticity usually the finite element method is used. The incompressibility of the elastic substrate and its thickness (finite thickness or half-space) are other factors in simplifying the

solution. By choosing an incompressible substrate the stiffening of the substrate with stretch that is an influencing parameter in cell response will be eliminated. The Green's function, which is by nature a 3×3 matrix, was calculated by Landau & Lifshitz (1984) known as the Boussinesq solution, and for isotropic half-space incompressible ($\nu = 0.5$) medium with tangential forces and displacement it is considered two-dimensional ($1 \leq i, j \leq 2$):

$$G_{ij} = \frac{3}{4\pi E r} \left(\delta_{ij} + \frac{x_i x_j}{r^2} \right) \tag{1.3}$$

where $r = |r|$ and δ_{ij} is the Kronecker delta equal to identity tensor I. The Green's function then is used in the following convolution integral equation where the traction force can be obtained by inverting the integral:

$$u(r) = \int G(r, r') f(r') dr' \tag{1.4}$$

The inverse solution can be done in Fourier space like Butler et al. (2002) where they developed Fourier transform traction cytometry (FTTC) or in real space by using boundary element method (Sabass et al., 2008).

The alternative solution in calculating the traction field is the direct conversion of the displacement field to the stress field. First, the displacement field u is converted to strain tensor ε using

$$\varepsilon_{ij} = 1/2 \left(\frac{\partial u_i}{\partial x_j} + \frac{\partial u_j}{\partial x_i} \right) \tag{1.5}$$

and the strain tensor is then converted to stress σ by using the following equation:

$$\sigma_{ij} = \frac{E}{1+\nu} \left(\varepsilon_{ij} + \frac{\nu}{1-2\nu} \varepsilon_{ll} \delta_{ij} \right) \tag{1.6}$$

Style et al. (2014) used the second method and solved the equation by Fourier transform in x and y for a finite thickness film. As for the case of embedded tracing particles within the substrate, while it is possible to use confocal microscopy to image all the embedded particles, tracing the particles and computing the strain tensor is time-consuming and can take up to 48 hours (Maskarinec et al., 2009) so it is more useful

for samples that are actually cultured inside a gel matrix (Koch et al., 2012).

To bring more insight into the role of cell-generated forces in lung cells' function and response to stretch this work aims to bring cell force measurement technique to stretching platform to facilitate the study of lung cells' traction forces in association with other stretch-induced responses.

Chapter 2

Methodology

2.1 Experiment set-up and substrates

The main requirement for TFM was the elastic substrate with fluorescent markers on which the cells were studied. For our experiments, the substrate was made of an ultra-soft biocompatible silicone gel, and red fluorescent beads were used as the markers dispersed on the surface of the silicone gel. As the analyzing software measures the traction stresses based on the thickness of the silicone gel, another layer of green beads was added at the very bottom of the silicone gel layer. The thickness was measured by measuring the vertical movement of the objective lens between the two focal plains. Depending on the requirements of each experiment, the fabrication process of the substrate slightly changed.

2.1.1 Materials

The silicone gel was made from DOWSIL™ CY 52-276; a two-component kit (A and B) of polydimethylsiloxane (PDMS) polymer. Sylgard 184, another form of PDMS in a kit consisting of the elastomer and a cross-linking agent was used to make the supporting membrane for the silicone gel in stretch experiments. The red fluorescent beads for the surface were purchased from Thermo Fisher Scientific (FluoSpheres™

Carboxylate-Modified Microspheres, 1 µm, Nile Red fluorescent (535/575), 2% solids) and green beads were from Lab 261 (0.5 µm Green Carboxyl Nano-spheres).

2.1.2 Substrate preparation

In all experiments, to achieve a uniform thickness of the silicone gel layer where all beads would be in one focal plain, silicone gel was spread by spin coating CY 52-276 mixture (Figure 2.1) on the supporting substrate which could be a petri dish, a glass cover slip or a silicon wafer.

Unstretched substrates. For experiments where cells were studied under shear stress, the structure shown in 2.2a was made on a 25×75 mm glass cover slip where a sticky–Slide I $^{0.8}$ Luer (ibidi, Cat. No. 80198) was attached on top. Similarly, for normal TFM a µ-Slide 8 Well (ibidi, Cat. No. 80806) was added on top of the cover slip. First, a solution of green fluorescent beads in ethanol was dropped on the glass cover slip that was treated in a plasma chamber for a few seconds with low intensity shortly before the dispersion of the beads. After ethanol completely evaporated, the silicone gel layer was made by spin-coating CY 52-276 mixture at 1000 r.p.m for 60 seconds and was left at room temperature to polymerize overnight. Since the the glue on the sticky-slide did not adhere properly to the polymerized silicone gel the sticky slide was slowly laid on the silicone gel right after it was spin-coated on the cover slip, and was then left to polymerize overnight to ensure a completely sealed binding and avoid any leaks during the experiment. Afterward, a solution of borate buffer containing the red fluorescent beads was added to the wells or channels. The buffer was removed 6-24 hours later and the remaining were washed with DI water. (Figure 2.2b)

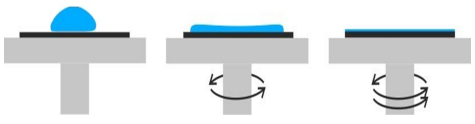

Figure 2.1: Spin coating is a process that uses the centrifugal force to deposit a uniform thin film on flat substrates by rotating the substrate at high speeds.

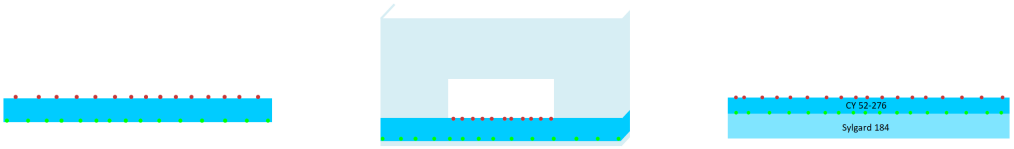

(a) (b) (c)

Figure 2.2: Schematic of substrate variations for each experiment. (a) shows the main components prepared (b) on a glass cover slip attached to µ-Slide, and (c) on an elastic membrane.

Double-layered membranes. For stretching experiments, the silicone gel layer was made on top of an elastic membrane (Figure 2.2c). The membrane was made using the stiffer form of PDMS, Dow Corning Sylgard 184, and by mixing the two components with a weight ratio of 1:10 cross-link agent to the elastomer, then degassed in a vacuum chamber for 30 minutes to completely remove the air. Then the mixture was spin-coated on a 3 inch silicon wafer that was previously coated with a hydrophobic compound (1,1,1,3,3,3-Hexamethyldisilazane) to avoid rupturing the membrane when being removed from the wafer. When stretched, both gel layer and elastic membrane got thinner so to avoid rupture and retain the stability of the structure it was necessary to make each layer thicker. In theory, reducing the speed of spinning results in a thicker layer but a speed lower than 1000 r.p.m compromises its uniformity while the thickness made at this speed was not enough. As a solution, both PDMS and silicone gel were made in three consecutive layers. PDMS mixture was spread on the wafer by spin-coating at 1000 r.p.m for 60 seconds and polymerized by heating at 65 ℃in the oven for 1 hour before repeating the same process. After the third layer of PDMS was made, the wafer was left in the oven overnight to secure a complete polymerization. Then the free surface of the membrane was plasma cleaned shortly and covered with few drops of green fluorescent beads in ethanol. After ethanol completely evaporated, CY 52-276 mixture was spin-coated at 1000 r.p.m for 60 seconds and left it at room temperature for 1 hour and this process, and after repeating the process 2 more times, the silicone gel was left at room temperature to polymerize overnight. Since the optimum working time of CY 52-276 mixture was 30 minutes and afterward, it started to polymerize, each gel layer had to be made from a freshly made mixture while for Sylgard 184 the working time was longer and the mixture could be kept in the refrigerator and used for

the second and third layers as well. Since the membrane was made on a flat surface, incubation of the red fluorescent beads was possible in two ways. First, the incubation could be carried out after the membrane was transferred and glued on the stretcher, but because the beads solution was not covered it would lead to the evaporation of the buffer and change of concentration. The second way that was used here was to incubate the beads while the membrane was still on the silicon wafer (Figure 2.3). A small petri dish (3 cm diameter, 5 ml volume) was filled with the solution to the maximum capacity. The wafer with the gel facing down was placed on top of the petri dish on one side and slowly laid down to avoid spilling the buffer and creating a bubble. After the edge of the petri dish was completely stick to the gel the wafer was flipped over and the buffer could incubate on top of the gel overnight. Next, the wafer was flipped over and carefully separated from the petri dish in the same way that was laid down. The remaining buffer was blow-dried and the membrane was removed from the silicon wafer and cut in a rectangle shape of 25×50 mm.

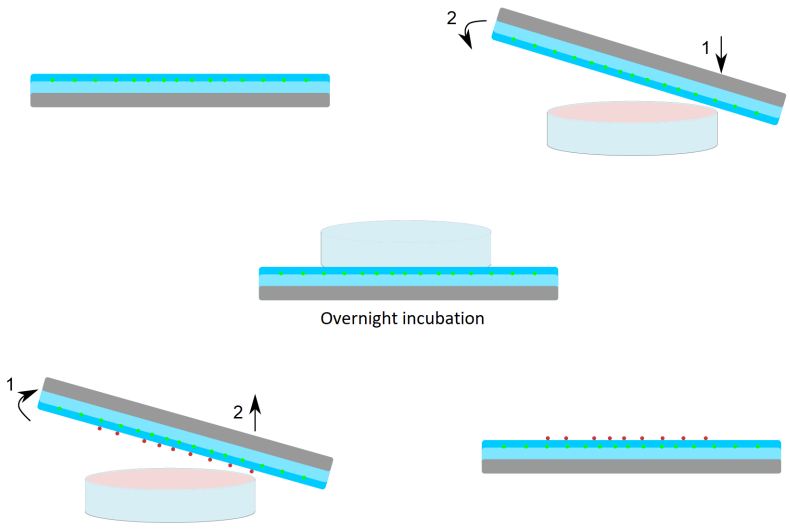

Figure 2.3: Incubation of fluorescent beads on the membrane.

2.1.3 Stretcher device

To attach the membrane on the stretcher first the distance between the two clamps was adjusted to 2 cm. To do so, the empty clamps were placed on pre-strain holders and the holders (not locked yet) on the plate rail were moved until the desired distance was reached. The holders then were fixed in place by locking screws to prevent further movement (Figure 2.4b). Using a silicone-based glue the membrane was sandwiched between the clamps, and before the glue completely dried, 2 small screws were used to fix the membrane and keep the clamps together. After the glue dried, a pre-strain was applied to give the membrane a nice flat surface for cell culture. This was done by increasing the distance between the pre-strain holders by 8 mm which resulted in a final 28 mm distance between the clamps. The clamps and membrane remain on the holders at all times without being removed during the cell culture preparation. The stretcher device in Figure 2.4a was mounted on the stage of an inverted microscope (Zeiss Axio Observer) (Gerstmair et al., 2009). At the beginning of each stretching experiment the distance between the stretcher's sliding blocks, where the clamps attach to the device, must be adjusted in order to fit the exact size of each membrane. First the clamps were inserted in the sliding blocks and then the pre-strain holders were removed. This was necessary to ensure that cells were not stretched or compressed before the start of experiment. After transferring the clamps/membrane, the device recorded the membrane's exact length and calculated the amount of elongation needed to provide our desired strain that was set in percentage.

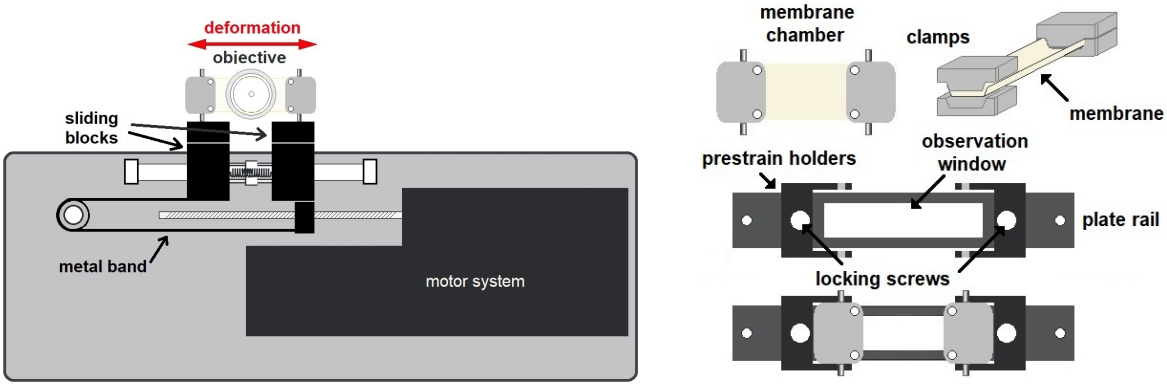

(a) (b)

Figure 2.4: (a) Stretcher device, (b) pre-strain holders and clamps.

2.1.4 Cell culture

The experiments were conducted using 3T3 mouse fibroblasts provided by Ulla Nolte (Institute of Experimental Physics, Ulm University) and human alveolar epithelial lentivirus immortalized cells (Kuehn et al., 2016) in wild type (hAELVi^{wt}) and their caveolin-1 knockout (hAELVi$^{cav-/-}$) provided by Prof. Frick and Kathrin Diem (Institute of General Physiology, Ulm University).

All cells were maintained at 37 ℃and 5% CO_2. 3T3 fibroblasts were maintained in Dulbecco's Modified Eagle Medium (DMEM) (Gibco) supplemented with 1% antibiotic/antimycotic solution (HyClone/Cytiva) and 10% FBS Gold Plus (Bio&Sell). hAELVi^{wt} and hAELVi$^{cav-/-}$ cells were maintained in huAEC-Medium (human Alveolar Epithelial Cell-Medium, InSCREENeX, Braunschweig, Germany) supplemented with 50 U/mL of penicillin and 50 µg/mL of streptomycin (Thermo Fisher Scientific) on the silicone gel coated with huAEC (human Alveolar Epithelial Cell) coating solution (InSCREENeX).

The cells were grown either in low density for single-cell experiments or high density for a confluent layer. As the last necessary step of TFM measurements, cells were remove from the silicone gel surface using Trypsin-EDTA solution (Sigma).

Patterns coating. In order to grow the cells on selected areas of the membrane, soft lithography samples were used to create strips of fibronectin and huAEC.

2.2 Experiment methods

2.2.1 CTF measurement without external stress

Traction forces of 3T3 fibroblasts, hAELVi^{wt}, and hAELVi$^{cav-/-}$ cells were measured in normal cell culture conditions. In addition, hAELVi^{wt} cells were also treated with 40 µM Blebbistatin and their traction forces were measured from before adding until 20 minutes after adding Blebbistatin. These measurements were performed on single cells.

2.2.2 CTF measurement under uniaxial external strain

The effect of external strain on single cell traction forces was investigated in two independent experiments:

I) stretching directly to 50% strain: first, a cell was chosen and its position was recorded in the controller software, then a bright field image and at the same time a fluorescent image of the red fluorescent beads were taken. Also, the silicone gel thickness below the cell was recorded by measuring the distance between the two focal planes of red and green fluorescent beads. Immediately after stretching the membrane to 50%, another bright field and fluorescent images were taken from the same cell together with a record of the silicone gel thickness. Then, cells were removed at the end of stretch using Trypsin. When the cells were completely removed, only a fluorescent image from red beads was taken. Using the software, the membrane was taken back to its original size before stretch (0%) and the objective lens was brought to recorded location of the cell, and a final fluorescent image of red beads was taken. The reason was that as a requirement for later analysis each fluorescent image taken from the cell location must be compared to another fluorescent image from the exact location without the presence of cell (reference image).

II) stretching to 50% strain but in three steps; first to 20%, then 35% and finally 50%: similar to the first method, a bright filed and fluorescent image of the unstretched cell were taken and thickness was recorded. Then the same thing was done after the first step of stretch (20%) before moving on to the next step. At the end of the third step (50%) cells were removed and a reference image was taken. The membrane was released in the same reversed steps as stretched so that separate reference images could be recorded for each step.

In another experiment the membrane with a confluent cell layer was stretched directly to 10% strain, 0.5% steps. This small stretch step was necessary because for this experiment each image was being compared to the 0% stretch image and with larger stretch steps the deformation would be too big to track the fluorescent beads. Same process was done on empty membranes that only with coating. Surface strain energy density was calculated using only the thickness of membrane at 0% state.

2.2.3 CTF measurement under fluid-induced shear stress

This experiment was performed on single cells using ibidi pump system (Cat. No. 10902). The chamber and perfusion set were prepared and connected according to ibidi instructions. Similar to stretch experiment, a bight field image of the live cell and a fluorescent image were taken before starting the flow of medium in the chamber. Further fluorescent images were taken in intervals of 5-60 seconds and a final image after removing the cells with Trypsin was taken as the reference image.

Prior to the experiment, the device had to be calibrated for the use of medium with viscosity of 0.01 with calibration factor of 1.38 that was calculated by following ibidi instructions. The flow for this set-up was 6 ml/min that would create a shear stress of approximately 1.3 dyn/cm^2 and then it was reduced to 1 ml/min flow rate with 0.22 dyn/cm^2.

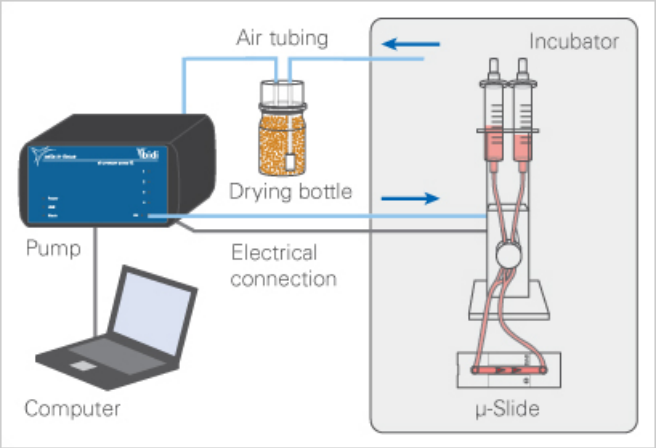

Figure 2.5: Perfusion set-up and pump system from ibidi. Image Source: Courtesy of ibidi GmbH.

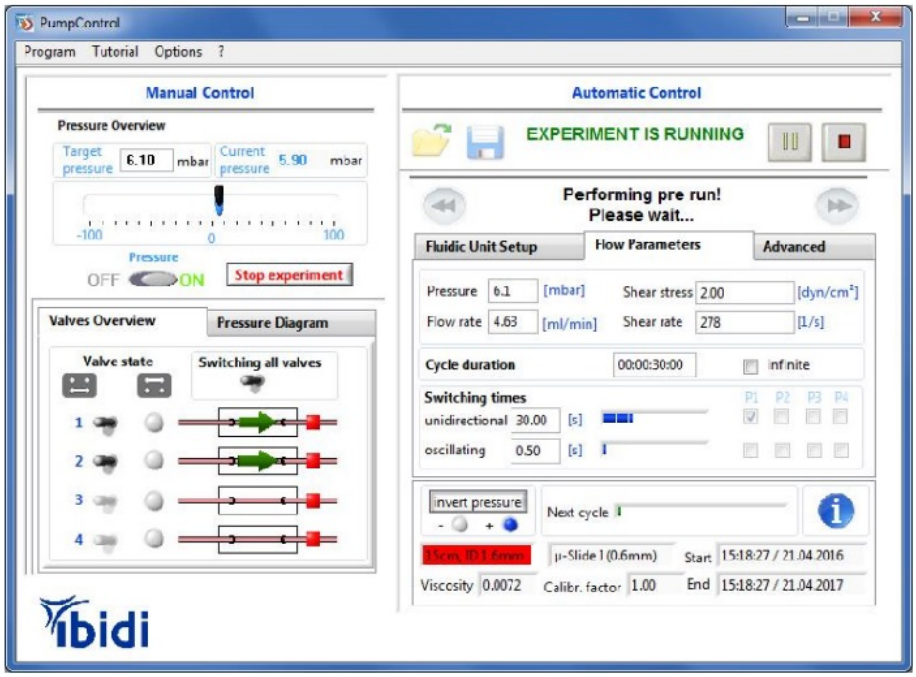

Figure 2.6: ibidi pump controller software. ibidi GmbH. (2022). PumpControl Instruction Manual. Image Source: Courtesy of ibidi GmbH.

2.3 Data processing

The analysis was based on measuring the silicone gel deformation caused by the cell. As a result of this deformation, it is expected that the red fluorescent beads on the silicone gel surface to appear in a different location when comparing the images taken during experiment to the reference image taken at the end of each experiment. A second software used this displacement to create a displacement field and convert it to a stress field.

To create the initial displacement field, different particle trackers were used including Particle tracker 2D/3D by Mosaic in ImageJ and two Matlab tracking codes, one developed by Rogers et al. (2007) and the other developed by Eric Dufresne and Daniel Blair. In both trackers, the position of each fluorescent bead on the surface of gel in each image is detected and recorded (Figure 2.7a and 2.7b) then through mathematical analysis the software conclude which positions throughout the series belong to the same bead (Figure 2.7c).

The poly-particle tracking code by Rogers et al. (2007) was based on the "Polyno-

mial Fit Gaussian Weight" (PFGW) method and could be run via a graphical user interface polyparticletracker_gui or command line function *data=polyparticletracker_gui;* in Matlab (Figure 2.8). The size of the particles to track could be adjusted in the interface and was set to 4 pixels with regard to the bead size and image resolution. The position of each particle is recorded in pixel of the entire image and suitable for tracking particles in complicated backgrounds. The code by Dufresne/Blair is suitable for tracking well-contrasted particles in simple images.

Traction Stresses were calculated using another Matlab code developed by Style et al. (2014) that could calculate the displacement field (Figure 2.7d) and transform it in to stress field (Figure 2.7e) for any given gel thickness and mechanical properties. Young's modulus was 5 KPa and Poisson's ratio was 0.499, and the thickness was measured as the distance between the red and green beads focal planes.

In time-lapse images (in flow experiments), all images were compared to a single reference image which would show the actual traction force in each frame. Alternatively, each image could be used as the reference image for its following image which would only show the change of traction force from one frame to the next. Using his code one could also calculate surface energy density, the feature that was used in the stretch experiment on the confluent cell layers.

The maximum of stresses for each cell was collected and presented as mean ± standard error (SE) using OriginPro 2017. For the test of significance Paired sample Wilcoxon signed-rank test was run for each comparison, with significance level of $p<0.05$ and $p<0.01$.

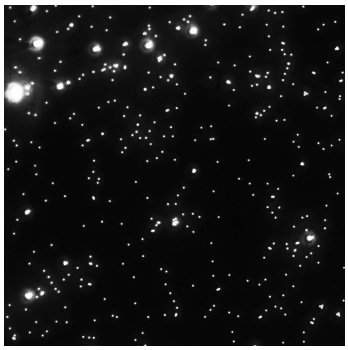

(a) Image with cell



(b) control image

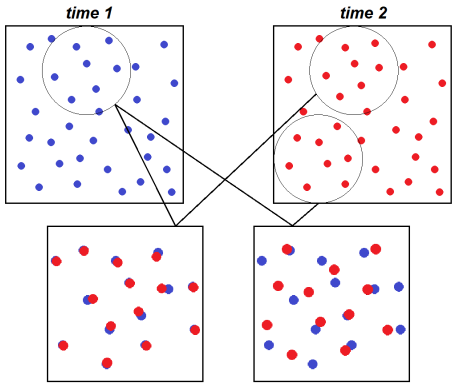

(c)

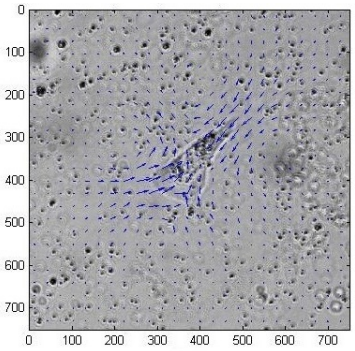

(d) Displacement field

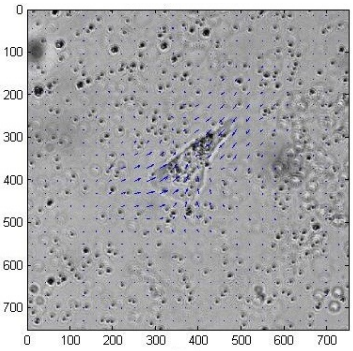

(e) Stress field

Figure 2.7: (a) and (b) fluorescent images taken from the beads before and after removal of the cell, (c) particle tracker decides which two beads are identical during the creation of displacement field (d) resulting in the stress field creation(e).

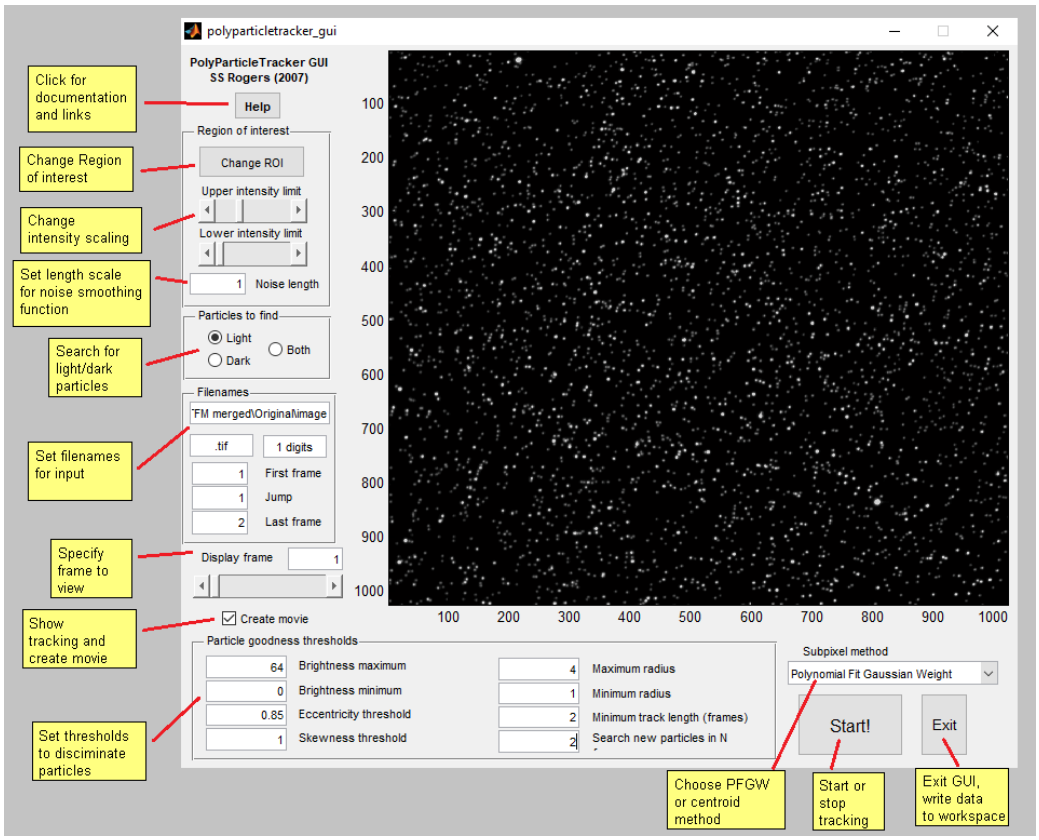

Figure 2.8: Graphical user interface for the poly-particle tracker by Rogers et al. (2007). The most important parameters are the radius, the file name that should be in the form of the address of the first image in the sequence, and the minimum track length that should be equal to the total number of images.

Chapter 3

Results

3.1 Membrane structure

Materials. At first, PDMS membranes were made only from Sylgard 184, where the fluorescent beads were right below the surface of the membrane. However, cells grown on these substrates created no detectable deformation despite their visible migration (Figure 3.1).

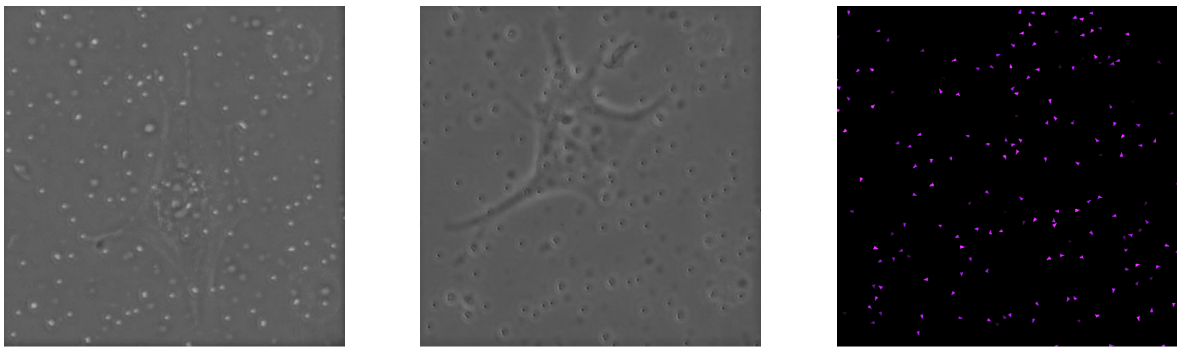

(a) (b) (c)

Figure 3.1: Bright field images of a 3T3 fibroblast cell on an un-stretched PDMS membrane made of Sylgard 184. All frames are showing the exact same spot on the membrane. Though the cell moved from position (a) to (b), no surface deformation was detected by the software (c).

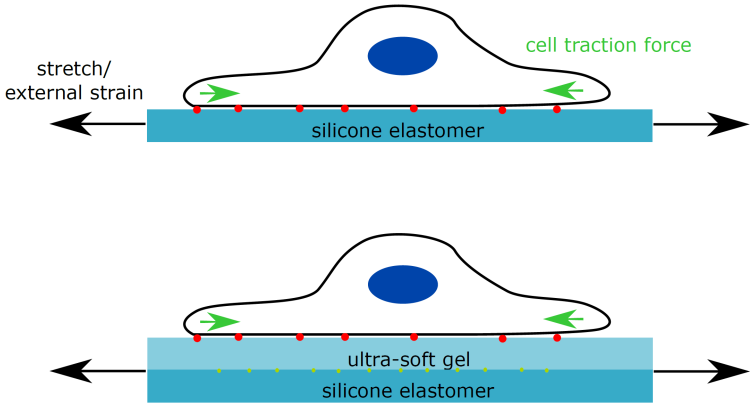

Figure 3.2: Schematics of the previous and new membrane design.

As a result, a silicone gel layer was added on top of the PDMS membrane where the deformation caused by cells could be detected, and the PDMS membrane would provide support and also facilitate stretching for this gel layer (Figure 3.2).

Fluorescent markers. For dispersion of the fluorescent beads on the main substrate different methods were tried with the aim to distribute the fluorescent beads on the same horizontal level so that they would all be on the same focal plane under the microscope. For membranes only made from PDMS elastomer, beads were mixed with the PDMS elastomer and spin-coated at high speed on top of a plain PDMS layer that was already polymerized, to create a thin layer where the beads would be on similar height because of the low thickness of the layer. Due to the high viscosity of the PDMS elastomer, this layer was not thin enough resulting in beads on visibly different focal planes and poorly distributed forming clumps and not mixing well with the elastomer. Therefore, PDSM and beads were diluted in n-Hexane to lower the viscosity and form a thinner layer. This resulted in the beads aggregating again because of their carboxyl coating and n-Hexane being hydrophobic (Figure 3.3a). As a solution, the membrane was made at first and then the beads were dispersed on top of it, then a highly diluted PDMS elastomer in n-Hexane was spin-coated at the end to form a thin layer covering the beads. The interaction of n-Hexane with the cured PDMS layer below it resulted in a wavy effect on the membrane and partial separation of the two layers after the solvent was evaporated (Figure 3.4) so the order of layer production was reversed to avoid this. Eventually, a uniform layer of PDSM was made with beads distributed on

the same level right below its surface. For the distribution of beads, simple evaporation deposition by diluting the beads in ethanol resulted in the formation of clusters and shrinking marks (Figure 3.3b), but when the PDMS surface was plasma-treated, it resulted in a nice distribution of beads without any clumps or shrink marks (Figure 3.2a and 3.3c). This process was also usable for distributing beads on other harder surfaces like glass and plastic.

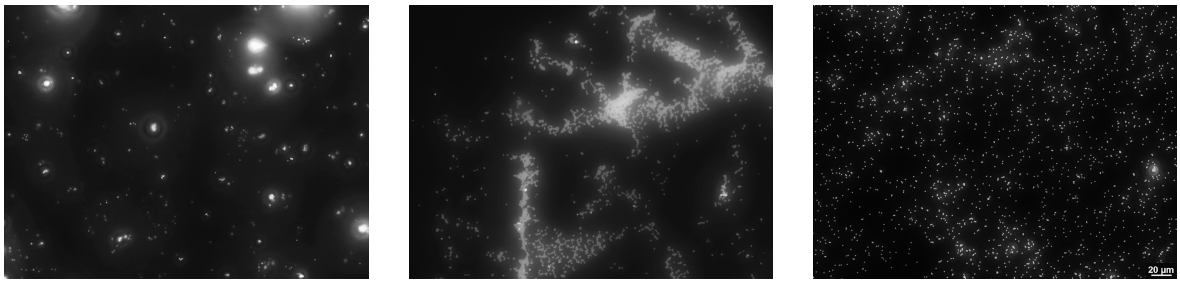

(a) (b) (c)

Figure 3.3: Fluorescent images of beads distribution. (a) mixing the beads with diluted PDMS; aggregated beads and beads on different focal planes were not suitable for our TFM technique. (b) beads shrink with the solvent as it evaporates, and adhere together in big groups. (c) a nice distribution of fluorescent beads, ideal for TFM technique.



(a) (b)

Figure 3.4: Wavy effect of n-Hexane the solvent of PDMS elastomer on polymerized PDMS and separation of the two PDMS layers.

The biggest disadvantage of this method, however, was that it was not compatible with the new silicone gel when we switched to the double-layered membrane (Figure 3.2b). The green beads at the bottom of the gel layer could be dispersed on the PDMS elastomer membrane using the above method, but the same method was not possible for the red beads. This was not a problem with beads distribution, but the effect

of plasma treatment on the silicone gel surface. Plasma treatment can increase the mechanical properties of the silicone gel enough to cause a significant change in the force calculations (Figure 3.15). In the end, the red fluorescent beads were distributed on the top surface of silicone gel without affecting its mechanical properties by using a low concentration of fluorescent beads in borate buffer that was incubated on top of the silicone gel layer instead of vapor deposition. As a result of several trials, a solution with 1.5 µl of bead stock per 1 ml of buffer at pH 6 was used. Despite having the same coating as 1µm beads, 0.5 µm beads did not distribute very well (Figure 3.5) and therefore were used for only marking the bottom of the gel layer. In general, a higher concentration of beads only resulted in less distribution with more and bigger clusters forming and . 1 µm beads distributed better with a buffer at pH 6 compared to pH 7.4 and 8.5 (Figure 3.6).

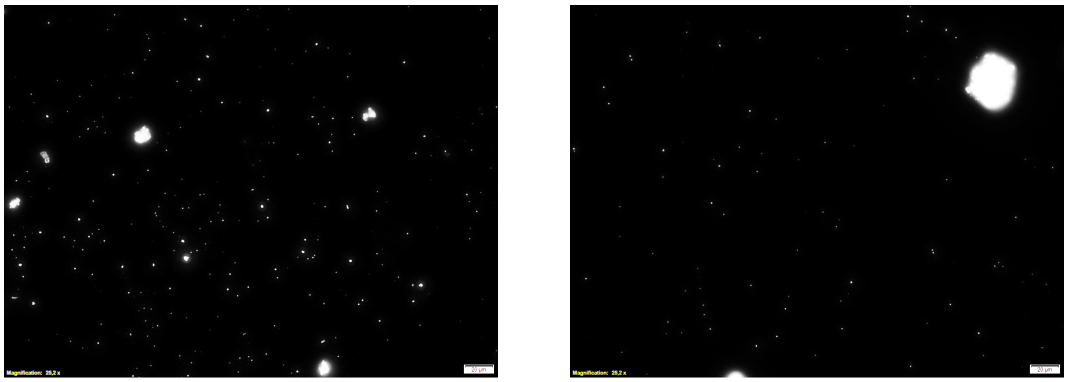

(a) pH 6

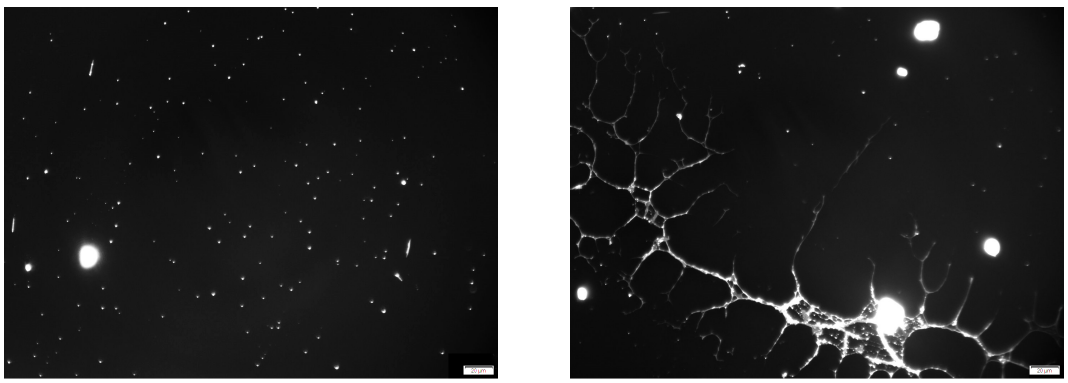

(b) pH 7.4

Figure 3.5: Distribution of 0.5 µm beads at 5 µl (left) and 15 µl (right) per ml of buffer.

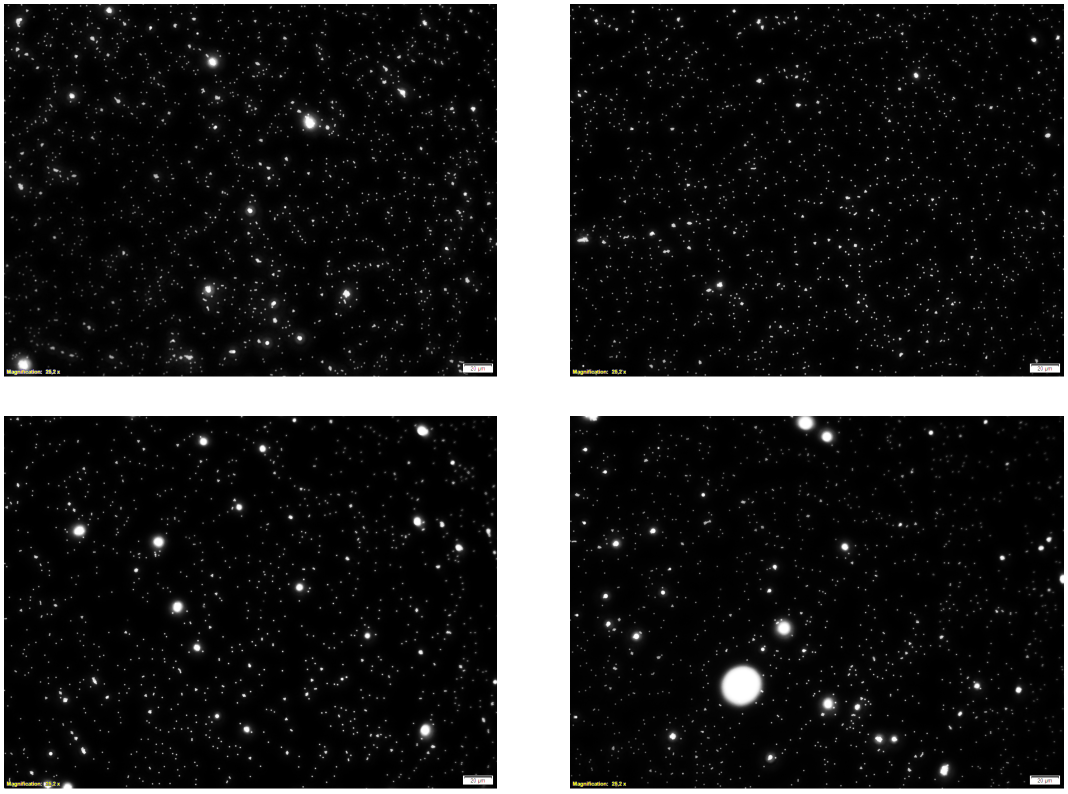

(a) pH 6

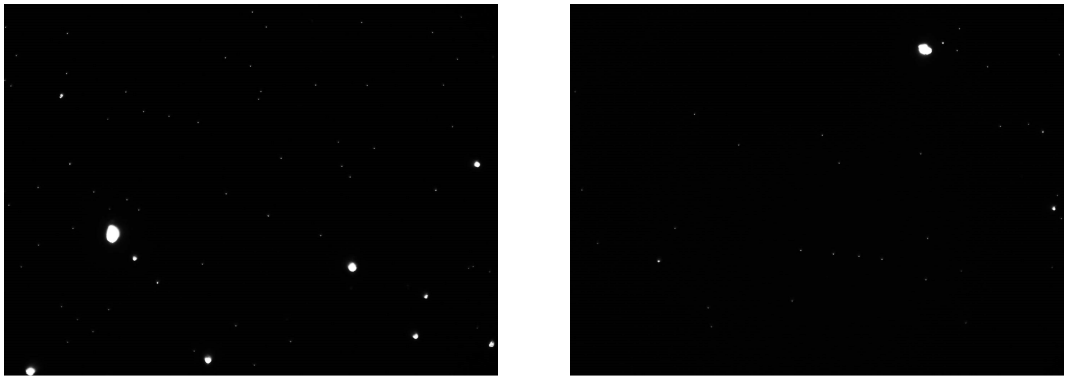

(b) pH 7.4

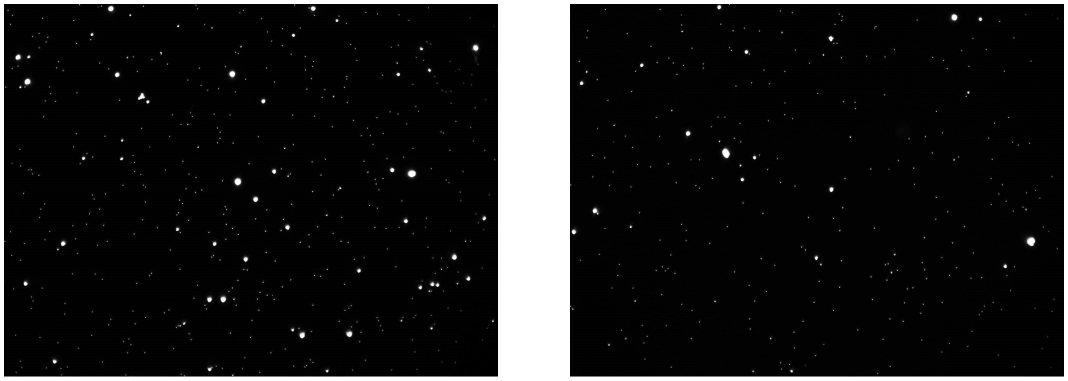

(c) pH 8.5

Figure 3.6

Membranes. During experiments, membranes broke due to different reasons. Choosing the right adhesives to attach the membranes to the stretcher clamps was crucial. Usually, the aquarium silicone adhesive is used, but it was one of the causes of membranes breaking so we replaced it with another silicone-based glue that was softer when it was dried. Furthermore, the membranes had to be cut cleanly without any imperfection on the edges or it would cause the membrane to break at higher strains. Another cause of membranes failure was the tightness of the clamps holding the membranes. This was the most challenging part because not having enough tightness on the clamps combined with the softness of the adhesive resulted in the membranes slightly slip between the clamps. Pipette tips were also responsible for a lot of broken membranes in the process of removing cells from the membranes. In one set of experiments an unusual phenomenon occurred; strange lines were visible in the unstretched membranes, and once 20% stretch was applied dark lines started to appear and grow from one side to the other side indicating a defect in the gel layer. The membranes were made according to protocol and it was not clear what caused the effect (Figure 3.7).

Imaging. Precisely leveled membrane with a uniform layer of the adhesive was also important for having a flat surface for imaging otherwise it would tilt the membrane resulting in partial visibility of the beads on the surface, and a thick glue layer became problematic at higher strains by causing the membrane to curve more resulting in a similar artifact (Figure 3.8). Having a low cell density in the cell culture was also an important factor since the TFM technique requires adequate free area around single cells (Figure 3.9).

Patterned coating. Preliminary results showed that fluorescent fibronectin coating strips of 200 µm width could be made using soft lithography stamps. Although the majority of cells had grown on the stripes, groups of cells adhered to other areas of the surface that were not coated (Figure 3.10). Similarly, hAELVi cells grew mainly on the patterns and partially on the area around the patterns (Figure 3.11a), with small forces detected on the strip the displacements on the strip were small (Figure 3.11b and 3.11c). Stretching to 10% strain traction stresses did not change (Figure 3.11d).

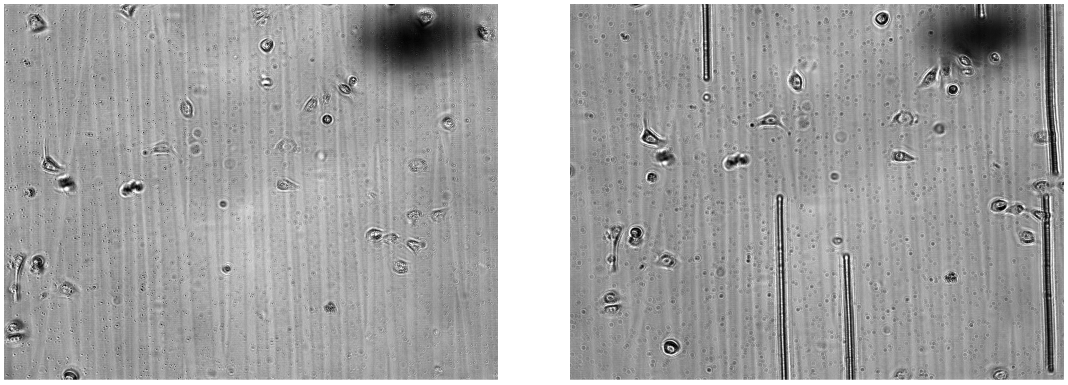

Figure 3.7: Defect growing in through the gel layer.

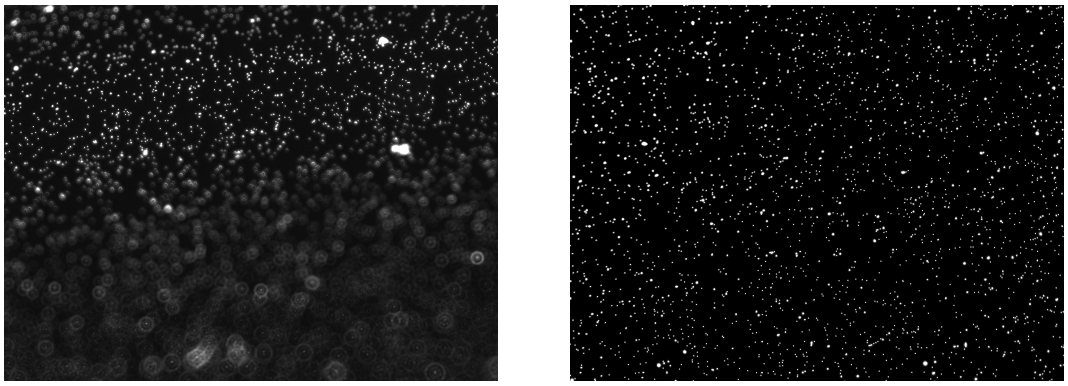

Figure 3.8: Partial visibility of the beads vs a precisely leveled membrane.

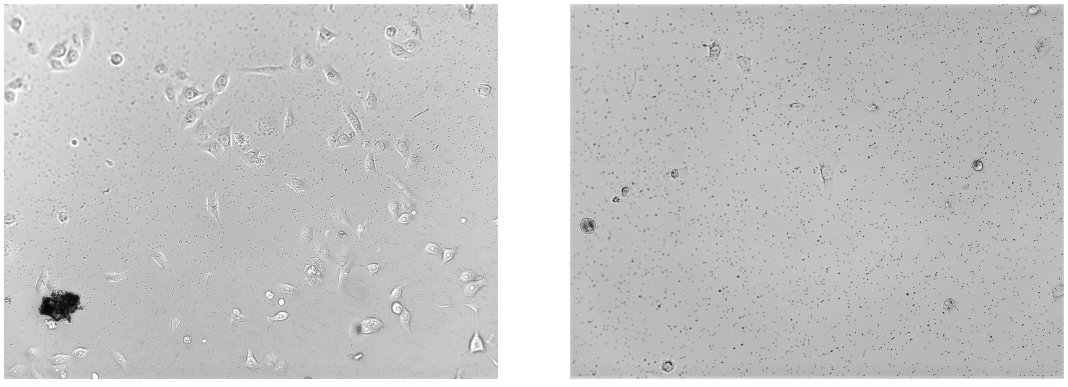

Figure 3.9: High cell density vs low cell density desired for TFM.

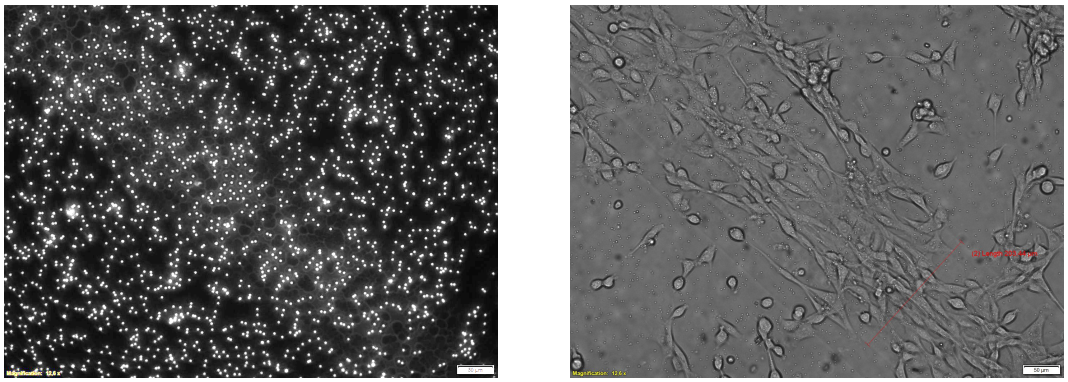

Figure 3.10: Fibroblast cells grown on a strip of fluerescent fibronectin coating.

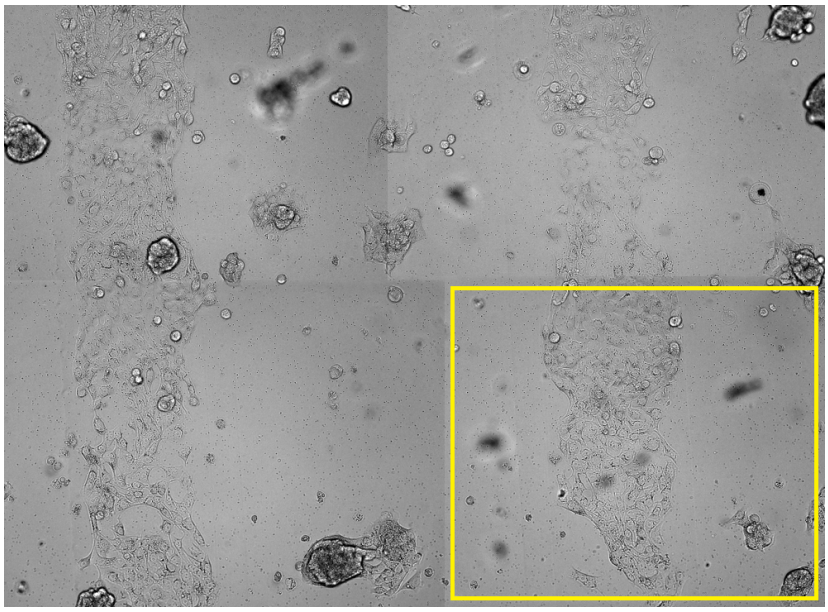

(a)

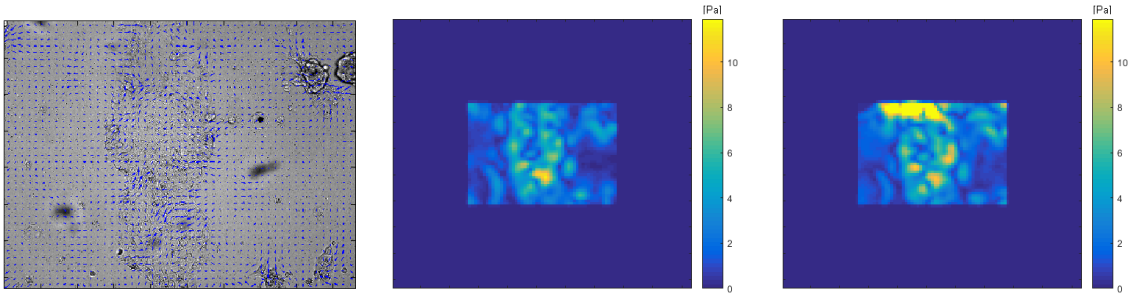

(b) (c) (d)

Figure 3.11: (a) Overview of the patterned area with hAELVi cells, (b) interpolated displacement, (c) traction before and (d) at 10% strain.

3.2 Image analysis

Drift. One necessary step before cell traction force calculation was the image preparation, including drift removal and cropping. Drift in image sequences was inevitable (Figure 3.12a) and had to be removed from the images otherwise all of the beads in the image appeared to have major displacement in the same direction which would contribute to the displacement field resulting in a false calculation of CTFs. Using a plugin in the image processing program ImageJ called *StackReg* (Thévenaz et al., 1998) the drift was removed and the true displacement could be detected (Figure 3.12b, 3.12c). The plugin has four types of transformation: *Translation, Rigid Body, Scaled rotation,* and *Affine*. Rigid Body and Affine were the transformations suitable for the simple drift in our images. Afterward, cropping the images in identical squares was required by the Matlab code as it would process the images in n×n matrix. This was done easily by editing tools of ImageJ where a sequence of images could be cut all at once.

Particle trackers. The first software used for traction force calculation were *FTTC* and *PIV* plugins developed by Tseng et al. (2012) designed for ImageJ. The iterative PIV plugin created the displacement field from the bead images, and the *FTTC* plugin reconstructed the stress field from the displacement data. Both these plugins had a plot function to visualize the displacement and stress field. *PIV* could track the movement of the beads and create the displacement field for samples with soft gel, however, it could not be used in traction force calculations because of the specification of *FTTC* plugin that assumes the gel layer is a half-space (Figure 3.13). This was in contrast to our objective of making thin membranes that would be getting even thinner when stretched. *Mosaic particle tracker 2D/3D* plugin in ImageJ also tracked the particles correctly but a particle tracker code written in Matlab was the better choice since the TFM calculating code was also written in Matlab and data transformation was easier. The code developed by Blair/Dufresne required more steps and had complicated parameters to set before tracking the particles, which could easily create irrelevant tracking data and traction forces (Figure 3.13c and 3.13f). On the other hand, *Poly-particle tracker* created better tracking results especially for smaller bead sizes and larger numbers of beads (Figure 3.13a and 3.13d). Despite the number of adjustable parameters for the Poly-particle tracker (Figure 2.8), the graphical interface

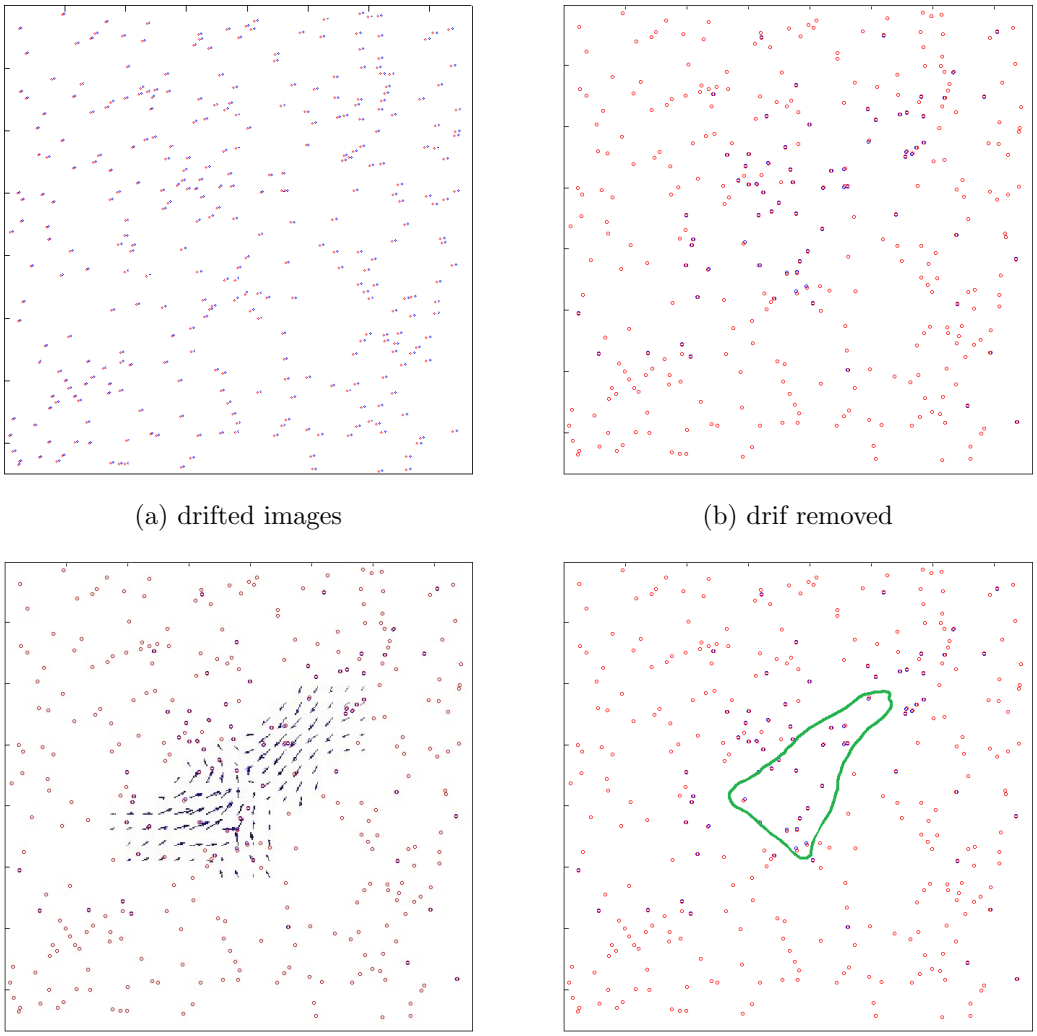

(a) drifted images

(b) drif removed

(c) interpolated displacement

(d) cell boundary

Figure 3.12: The overlap of the positions of beads detected in two fluorescent images of beads. Red spots show the position of beads in the control image, and blue spots indicate the beads in the cell image. (a) All beads seem to have moved due to the drift in images, and (b) shows the actual movement of beads after drift is removed with StackReg resulting in the creation of a displacement field (d). Marking the cell boundary (d) shows the detected displacement of beads to be relevant to cell location

was easy to use and most parameters had default settings, and it was accessible via only one line of command. The only thing was to transfer the output data to the TFM code. The data were created in a structure with three fields containing various information about each detected bead while the TFM code required only the x and y position of each bead in a specific arrangement. Additional coding was needed to extract the information from the Poly-particle tracker and rearrange them for the TFM code to use (Appendix B).

Particle tracking for calculation of Surface Strain Energy Density of stretched membranes was only possible when the images were taken every 0.5% stretch step otherwise large displacement of the beads would result in false tracking. Figure 3.14a shows the superimposed images of a membrane taken during a stretch, and the blue circles in Figure 3.14b show each detected and tracked bead. The problem here was that if a bead was not detected in one image the chain of the tracked bead would break and it would not show up in the final results. This can be seen in Figure 3.14 as some of the white tracks are not shown with blue circles.

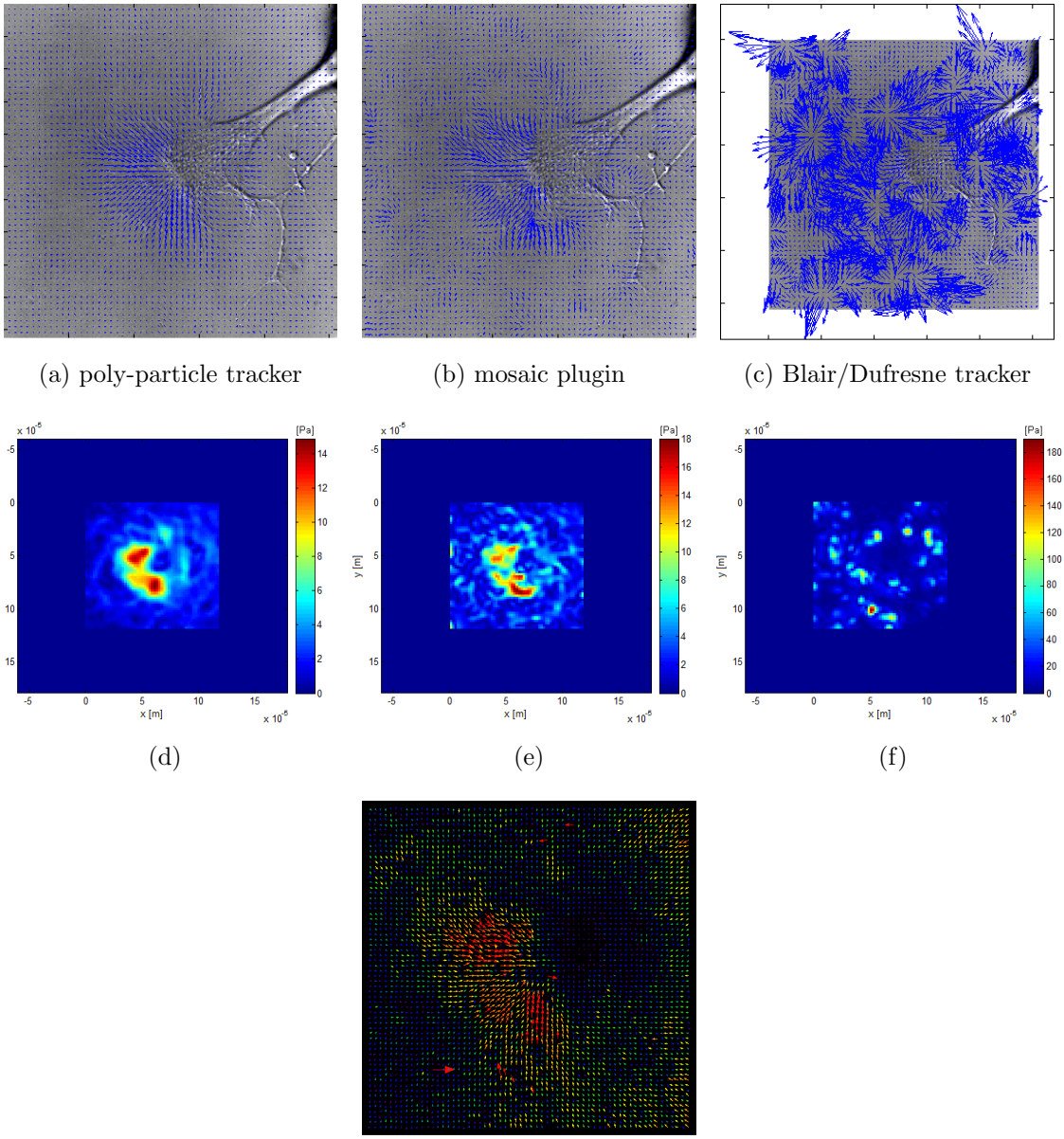

(a) poly-particle tracker (b) mosaic plugin (c) Blair/Dufresne tracker

(d) (e) (f)

(g) PIV

Figure 3.13: Comparison between tracking results and displacement field created by (a) poly-particle tracker, (b) Mosaic particle tracker 2D/3D plugin, and (c) Blair/Dufresne tracker on a sample image. (d), (e), and (f) stress field calculations based on the displacement fields of (a), (b), and (c), respectively, emphasizing the importance of particle tracking quality when generating the stress field. (g) Tracking by PIV plugin on the same sample image.

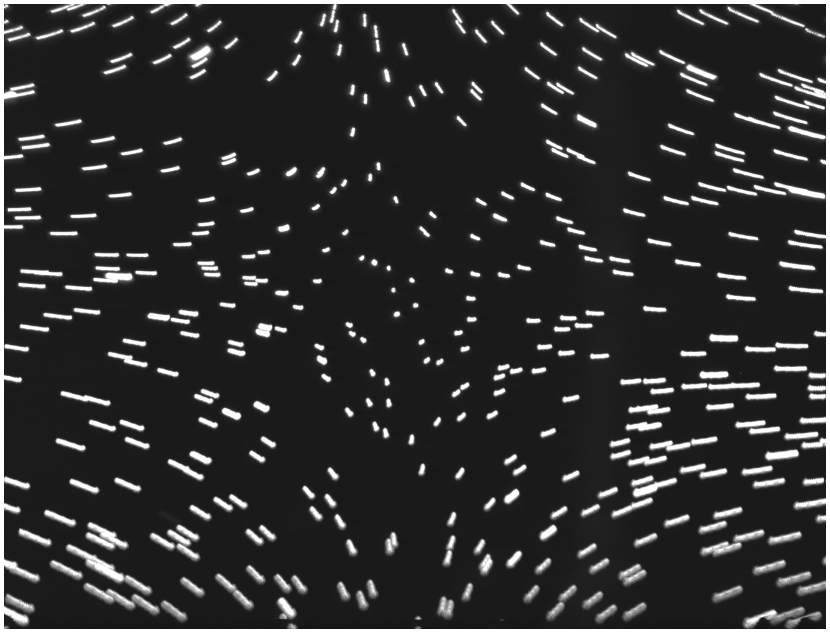

(a)

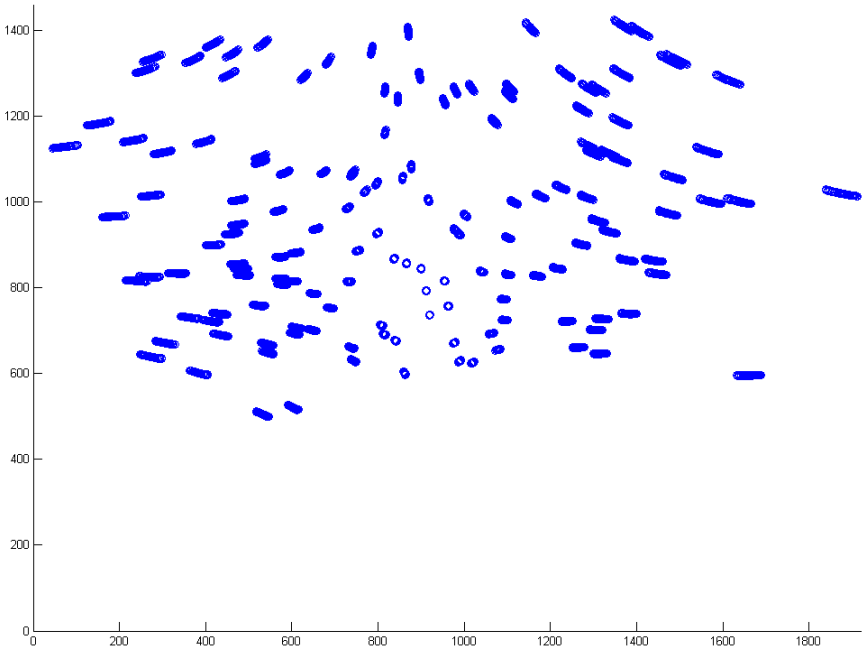

(b)

Figure 3.14: Tracking of beads on a stretched membrane. Tracking only possible with frames taken every 0.5% strain giving a total of 21 frames for stretching from 0% to 10%.

3.3 Cell traction force measurements

3.3.1 CTFs of unstretched cells

Traction force microscopy of cells grown on silicone gel substrates shows a significant drop in measured total traction forces of cells grown on a plasma-treated gel compared to that of cells grown on non-treated gel. These results indicate the huge effect of plasma treatment on the mechanical properties of the silicone gel (Figure 3.15).

The comparison between the total traction forces of hAELVi^{wt}, hAELVi$^{cav-/-}$, and 3T3 cells grown on normal gel substrates (Figure 3.16) shows that hAELVi$^{cav-/-}$ cells generated considerably higher forces than hAELVi^{wt} cells while 3T3 cells generated forces in the range slightly higher than the wild type ATI and lower than the cav-1 knockout ATI cells.

Traction forces of hAELVi^{wt} cells that were treated with 40 µM Blebbistatin immediately started to decrease, and were significantly lower 20 minutes following the treatment (Figure 3.17).

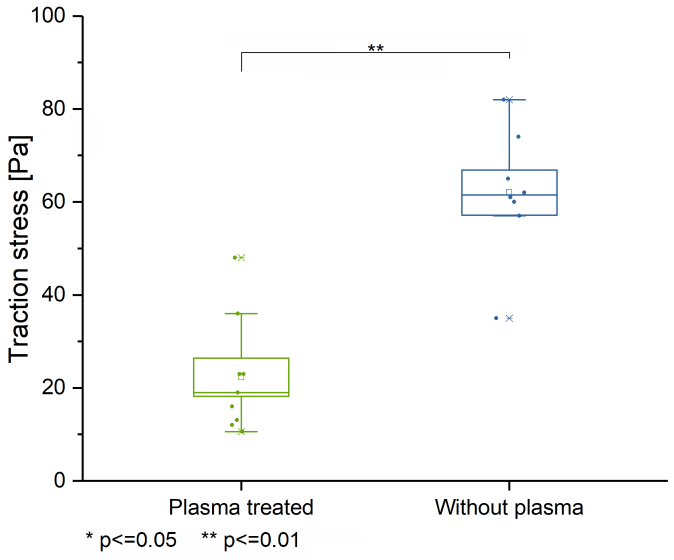

Figure 3.15: Total traction forces of cells grown on plasma treated in comparison with the forces measured for cells on non-treated control substrate (n=8).

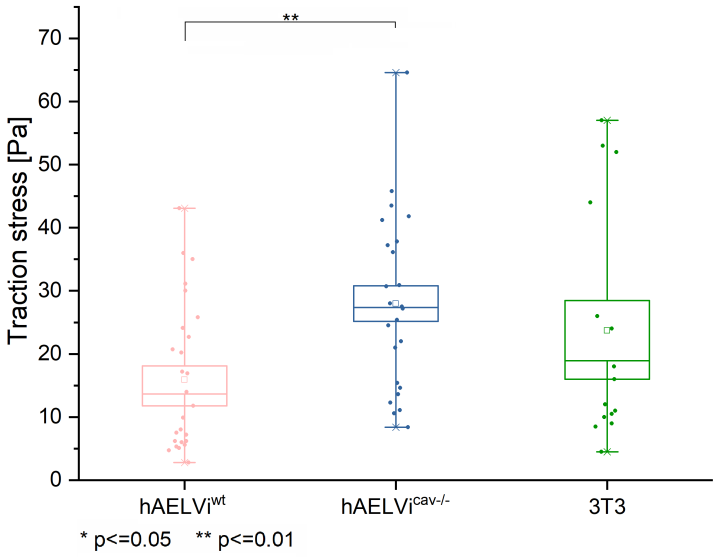

Figure 3.16: Total traction forces measure for hAELVi^{wt} (n=27), hAELVi$^{cav-/-}$ (n=24), and 3T3 fibroblast cells (n=15).

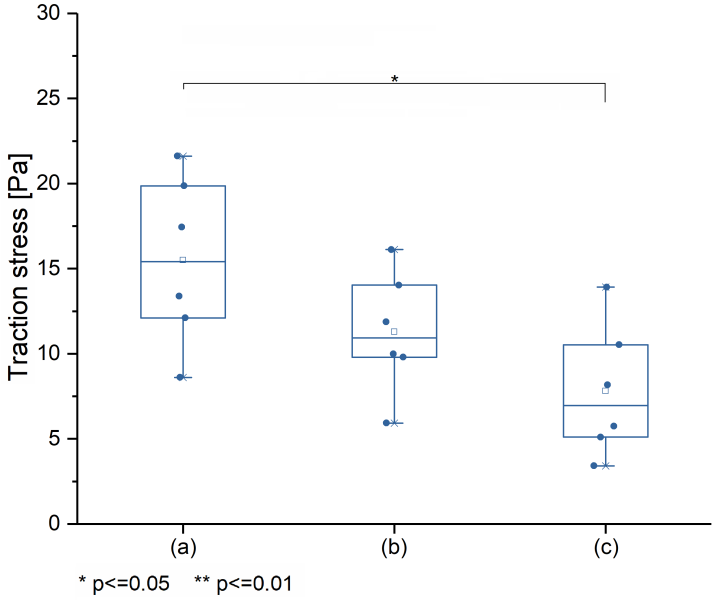

Figure 3.17: Total traction forces measurements for hAELVi^{wt} cells (a) without, (b) immediately after, and (c) 20 minutes after Blebbistatin treatment (n=5).

3.3.2 CTFs of uniaxially stretched cells

In this experiment, one group of cells (hAELVi^{wt} or hAELVi$^{cav-/-}$) were subjected to a sudden uniaxial stretch to 50% strain while a second group of the same cell type were stretched in three smaller intervals leading to 50% strain and with ~2 minutes delay between each interval.

During these experiments, the gel thickness had to be measured separately for each step where errors could occur especially when the gel layer was getting thinner. To solve this problem, Poisson's ratio of the silicone gel as an incompressible material was used to calculate the change of thickness for each known strain size (Appendix A). The majority of the thickness measurements during the experiments were similar to these calculations and in the exceptional cases, the faulty measurements were replaced with the calculated values.

In addition to the calculation of total traction forces, the TFM code also separated the forces in X and Y directions which with consideration to the stretcher setup, traction forces in the direction of the stretch axis are labeled with X, and forces parallel to the transverse compression are labeled with Y. (Figure 3.18).

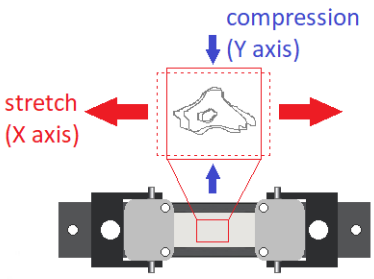

Figure 3.18: Stretch direction in relevance to image axis and force labeling.

hAELVi^{wt} cells response to 50% strain

The total traction forces of cells increased in both groups with cells experiencing the gradual strain showing more increase. The traction forces in the direction of stretch also increased and for cells experiencing a sudden strain, this increase was more significant compared to cells experiencing a gradual strain. The traction forces in the transverse direction decreased as was expected due to the compression of the substrate. This drop, in the transverse forces, was more significant for the cells undergoing the sudden strain while in most of the cells experiencing the gradual strain, transverse forces did not show considerable change in between the intervals (Figure 3.19).
In the first step of stretch to 20% strain, the total traction forces as well as in both directions dropped which the total traction forces and in stretch direction increased in the next following intervals while the transverse forces remained relatively unchanged. hAELVi^{wt} cells subjected to the sudden strain that remained in the stretch position exhibited stress relaxation during 10 minutes (Figure 3.20).

hAELVi$^{cav-/-}$ cells response to 50% strain

In contrast to the wild type cells, the total traction forces of cells decreased in both groups with cells experiencing the sudden strain showing a more significant decrease. The traction forces in the direction of stretch also decreased and again, for cells experiencing a sudden strain this decrease was more significant compared to cells experiencing a gradual strain. It is also notable that hAELVi$^{cav-/-}$ cells compared to the wild type cells exhibited significantly higher forces before the stretch which is in line with the results in Figure 3.16.
hAELVi$^{cav-/-}$ cells undergoing the sudden strain also had a significant drop in the transverse forces as was expected. However, the cells subjected to the gradual strain showed a different pattern in their transverse forces compared to the wild type cells; transverse forces also significantly reduced in the first two intervals (Figure 3.21).

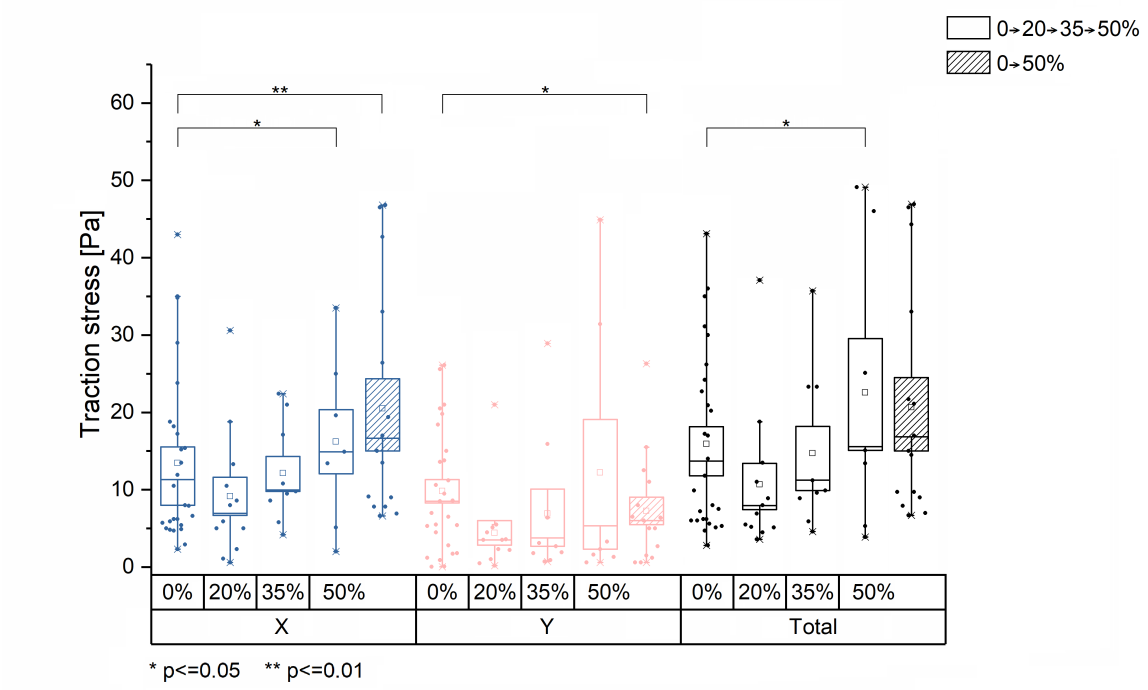

Figure 3.19: Traction forces generated by hAELVi^{wt} cells per unit area. The box at 0% represents the forces in the unstretched phase before applying the strain. Plain boxes represent the forces during three stretch intervals to 50% while the shaded box represents the forces during a sudden increase of strain to 50%. Forces are shown in total amount, in the direction of the stretch and the transverse direction ($7 \leq n \leq 15$).

Cell area and detachment from the substrate

Both hAELVi^{wt} and hAELVi$^{cav-/-}$ cells had similar cell area in unstretched phase (Figure 3.22), however, during the two stretch patterns their cell areas changed completely in an opposite manner. In most hAELVi$^{cav-/-}$ cells partial detachment from the substrate could be easily observed (Figure 3.23).
Figure 3.24 shows that 79% of hAELVi^{wt} cells had larger areas meaning no or insignificant detachment while 87% of hAELVi$^{cav-/-}$ cells had smaller areas indicating partial detachment from the substrate.

The changes in the cell areas shown in Figure 3.25 indicate that the size of the increase in the area of hAELVi^{wt} cells was significantly smaller than the size of the decrease in the area of hAELVi$^{cav-/-}$ cells. Furthermore, the size of changes as well as the number of cells exhibiting these changes was different depending on the stretch experiments.

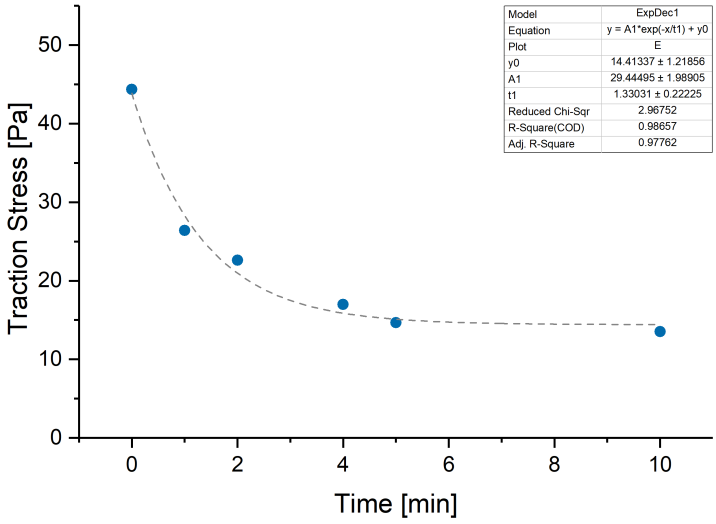

Figure 3.20: Stress relaxation of hAELVi^{wt} cells during 10 minutes of 50% static stretch.

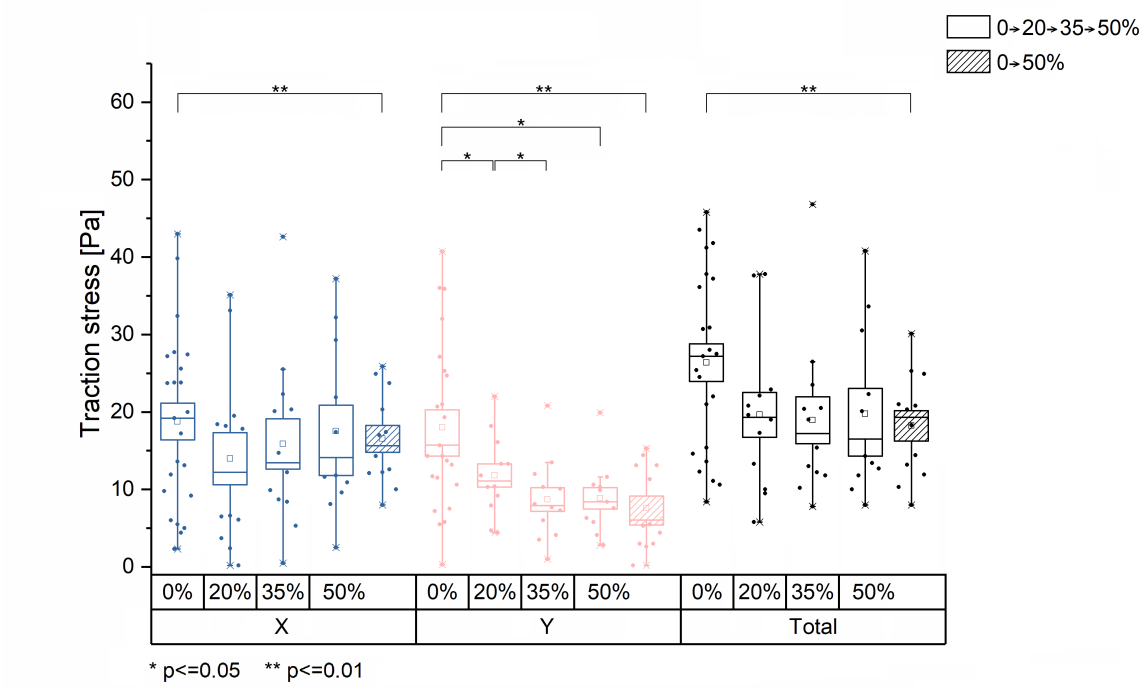

Figure 3.21: Traction forces generated by hAELVi$^{cav-/-}$ cells per unit area. The box at 0% represents the forces in the unstretched phase before applying the strain. Plain boxes represent the forces during three stretch intervals to 50% while the shaded box represents the forces during a sudden increase of strain to 50%. Forces are shown in total amount, in the direction of the stretch and the transverse direction ($11 \leq n \leq 12$).

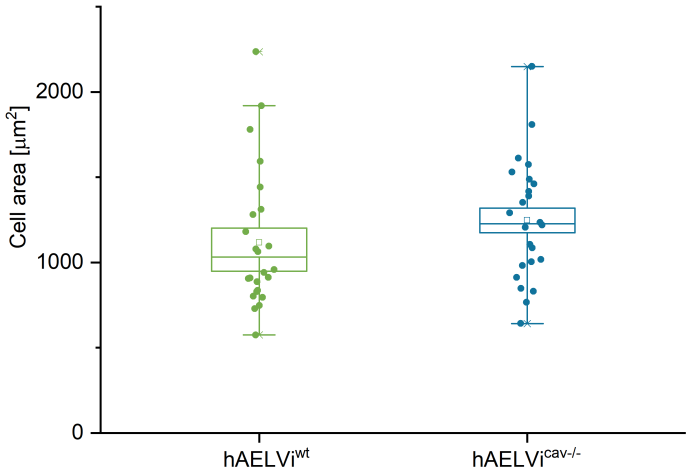

Figure 3.22: Cell area of hAELVi^{wt} and hAELVi$^{cav-/-}$ cells in the unstretched phase.

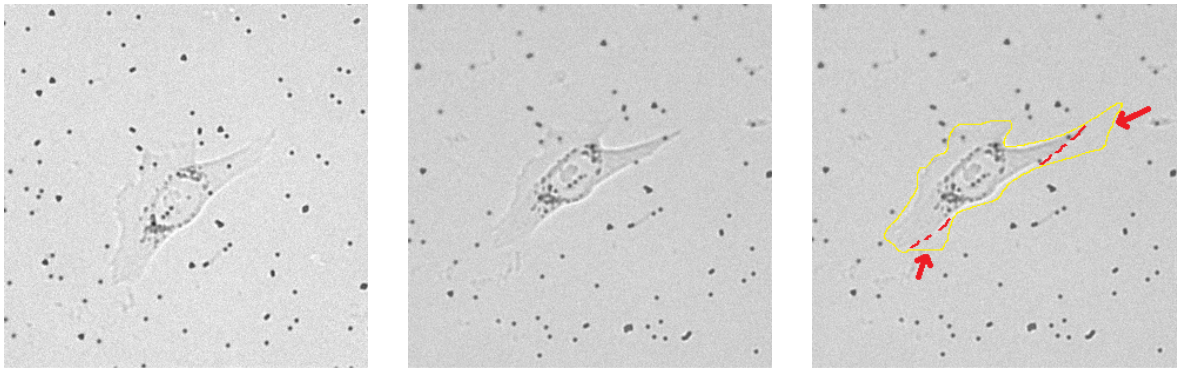

(a) (b) (c)

Figure 3.23: Partial detachment of a hAELVi$^{cav-/-}$ cell: (a) the unstretched phase, (b) under 50% strain, and (c) comparison of the cell boundary; the red dashes show where the cell was detached.

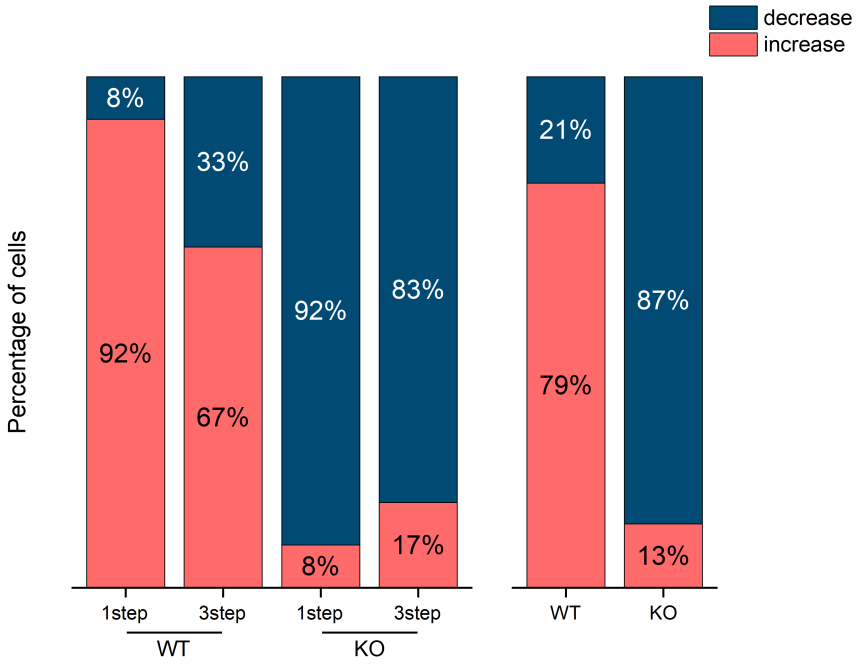

Figure 3.24: Percentage of cells of each type showing an increase or decrease in their areas. Most hAELVi^{wt} (WT) cells expanded with the stretch while most hAELVi$^{cav-/-}$ (KO) cells partially detached from the substrate.

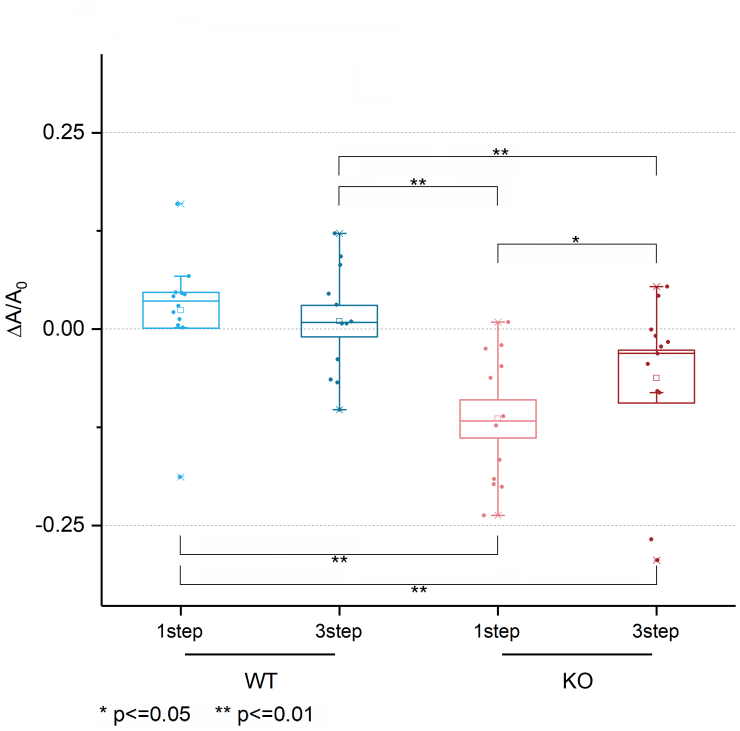

Figure 3.25: Changes of the cell areas relative to the area of cells in the unstretched phase.

Confluent cell layer with 10% strain

The surface strain energy of the silicone gel calculated for membranes with confluentl layer of hAELVi^{wt} cells showed no significant difference from the surface strain energy of empty membranes under same stretch condition (Figure 3.26).
However, the surface strain energy was similar to the theoretically calculated strain energy for stretching a bar of the same mechanical properties and size as the gel layer (Figure 3.27).

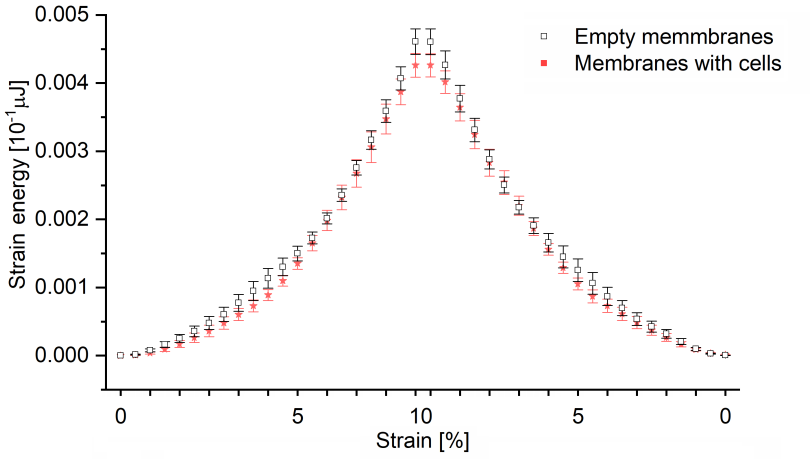

Figure 3.26: Strain energy density of empty membranes and membranes with a confluent layer of hAELVi^{wt} cells (n=6).

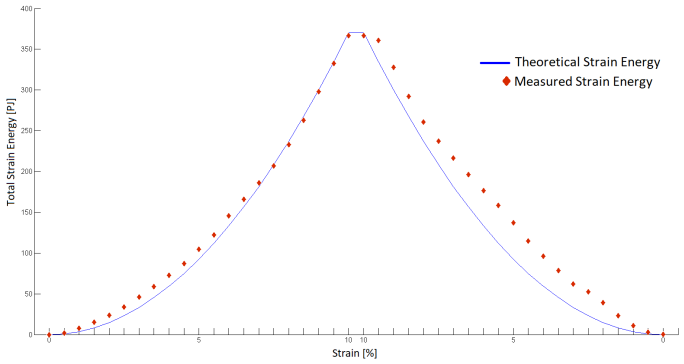

Figure 3.27: Strain energy [pJ] of a membrane stretched to 10% strain (red markers) in comparison to theoretical calculation.

3.3.3 CTFs of cells under fluidic shear stress

During the flow experiments, no changes in the direction of cell traction forces was observed. The time laps images indicated the detachment of cells as they constantly dropped. Under shear stress of 1.3 dyn/cm^2, the cells were removed in less than a minute. Although the cells were not removed under the lower shear stress of 0.22 dyn/cm^2, the traction forces continued to drop and the cells were removed even after the flow had stopped (Figure 3.28 and 3.29). In addition, fluid leaking from the sides of the chamber was another drawback that resulted in the change of chamber assembly.

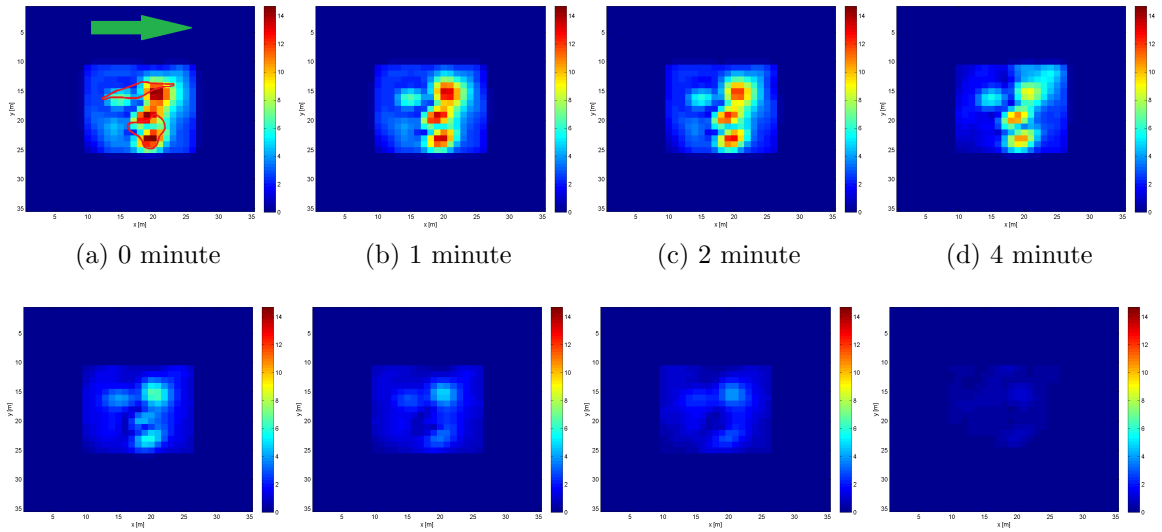

(a) 0 minute (b) 1 minute (c) 2 minute (d) 4 minute

(e) 6 minute (f) 8 minute (g) 10 minute (h) 17 minute

Figure 3.28: Cell traction forces under shear stress during 10 minutes reducing constantly. Green arrow shows the flow direction.

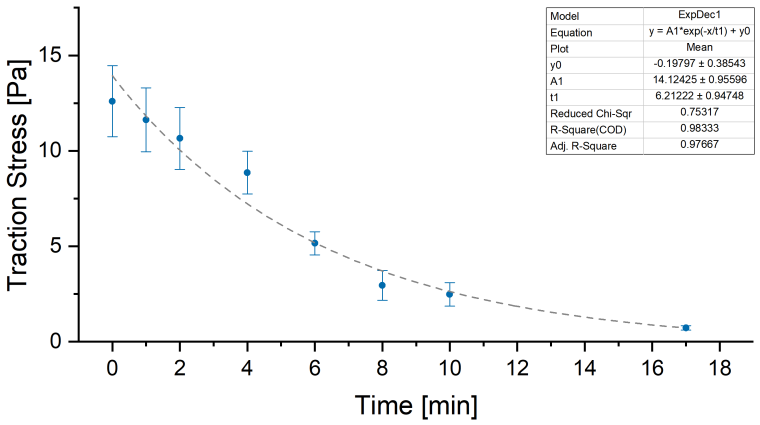

Figure 3.29: Cell traction forces dropping under the shear stress within 10 minutes.

Chapter 4

Discussion

4.1 Methods overview

PDMS is considered a flexible material, however, with Young's modulus of 1.72 MPa (Palchesko et al., 2012), this polymer is not soft enough to be deformed by cells. Silicone gel on the other hand, though being ideal for the TFM technique, can not be made into a stretchable membrane. These led to the change in the membrane design to create double-layered membranes that were in this work.

Since the fluorescent beads provide data regarding the deformation, using smaller-sized beads, higher resolution for the final displacement and traction stress fields can be achieved. Because of the limitations on the fluorescent wavelengths suitable for the microscopy, and the size of the manufactured beads, in the end, 1 µm beads were used which are relatively larger and can be easily seen in all the bright field images. Unfortunately, smaller beads with the desired wavelength purchased from another manufacturer failed to distribute properly on the gel substrate.

The fabrication method of membrane and the advantage of the TFM Matlab code over the FTTC plugin of ImageJ, make it possible to produce membranes with any thickness depending on the experiment requirements possible. FTTC is still a useful method for normal traction force microscopy when a membrane or a relatively thin gel layer and thickness measurements are not needed.

4.2 Experiments results

4.2.1 Traction forces of unstretched cells

Blebbistatin is a potent myosin II inhibitor, and it has been shown to reduce the traction forces of fibroblasts in 30 minutes (Beningo et al., 2006). Here, the similar response from hAELVi^{wt} cells with their traction forces immediately dropping indicates the significant role of myosin II in traction force generation in ATI cells.

Caveolae association to actin through Cav1 -as one of the main components of the caveolar structure- has been proven for a long time (Rothberg et al., 1992; Stahlhut & van Deurs, 2000), however, their role in multiple mechanotransduction pathways is still the subject of recent studies (Buwa et al., 2020; Gilbert et al., 2016). Since caveolae are abundant in cells that experience mechanical stress such as ATI cells, and their association to actin as well as cytoskeleton regulating pathways (Burridge & Wittchen, 2013; Kaunas et al., 2005) they seem to be involved in cell response to mechanical cues. Grivas et al. (2020) measured the elasticity of zebrafish cardiac cells and showed that there was a significant decrease in the elasticity of Cav1 knockout cardiac cells and they exhibited higher stiffness compared to the wild type. N. Wang et al. (2002) and Lam et al. (2012) found that the cells with higher stiffness have higher pre-stress (which is the traction force in the unstretched phase).
Considering these findings, the significantly higher traction forces we measured for the hAELVi$^{cav-/-}$ cells than that of the hAELVi^{wt} cells are in line with these studies. Since cell stiffness measurement was not part of this work, there are no data supporting the idea that hAELVi$^{cav-/-}$ cells were stiffer, however, with the assumption that our hAELVi$^{cav-/-}$ are stiffer due to the lack of Cav1, their higher pre-stresses compared to hAELVi^{wt} cells are justified.
Furthermore, in a study by (Moreno-Vicente et al., 2018) it was shown that cell proliferation in response to substrate stiffness was modulated by Cav1 through actin-cytoskeleton-dependent mechanisms, and another study by Han et al. (2012) showed that substrate stiffness can have a strong influence on traction force. Taken together, this could mean that the lack of Cav1 either affects the assembly of the actin filaments in its response to substrate stiffness or cause disruption in the sensing function of actin

of the environment, both of which could result in a change of cytoskeleton stiffness. The disrupted sense of environment can also help to make sense of the response of these cells in our stretch experiments.

4.2.2 Traction forces of stretched cells

hAELVi^{wt} cells response to 50% strain

The changes observed in the traction forces of the cells undergoing a sudden stretch to 50% strain are in line with previous studies. The increase in total traction force is consistent with findings of other studies that suggested the cell contractile forces and stiffness increase with stretch (Mann et al., 2012; Trepat et al., 2007; Rosowski et al., 2018; Asmani et al., 2019; N. Wang et al., 1993). The reduction of transverse forces was expected because of substrate compression. A stress fiber in this situation can be compared to a spring in a pre-stretched condition where with a sudden decrease of the distance between its two ends the tension drops. Furthermore, in a study by Costa et al. (2002), it was shown that a rapid compression of the substrate after a short stretch resulted in buckling of cytoskeletal filaments aligned in the same direction. Although in our experiment there was only transverse relaxation without previous stretch, for the stress fibers oriented in that direction, a substrate relaxation would resemble a release after a long-term stretch and we should still expect some buckling effect which means reducing the tension in those stress fibers. Rosowski et al. (2018) showed that traction forces of fibroblasts subjected to a stretch for 10 minutes where their traction forces had already reached a plateau value within the first 100 seconds of the stretch, dropped below baseline force upon substrate release. This has been shown also by Chen et al. (2010) where they related this response to rapid actin disassembly and fluidization of the cell. Krishnan et al. (2009) also observed rapid depolymerization of the actin filaments during the stretch relaxation of their experiments that could account for the decrease in the transverse forces in our results. Although in our experiment there was only transverse relaxation without previous stretch, for the stress fibers oriented in that direction, a substrate relaxation would resemble a release after a long-term stretch and we should still expect some buckling effect which means reducing the tension in those

stress fibers. For this reason, the orientation of cells in the unstretched phase becomes decisive in how the cells respond. In regard to the total traction forces, despite not being considered a significant increase statistically, this increase is due to the increase of traction forces in the direction of the stretch that is affected by the drop in transverse forces, resulting in a less significant increase. This shows the importance of looking into the traction forces in the two directions separately for a more sensible interpretation of the results. In response to the gradual stretch, the traction forces along the stretch axis and the total forces gradually increased to a final significant amount at 50%. Although this increase was less than the increase in response to the sudden stretch, it is consistent with the first experiment. The difference between the two experiments is that the transverse forces did not change significantly after the small drop in response to 20% strain which can be related to the duration of the experiment. Costa et al. (2002) reported rapid remodeling of the actin stress fibers within $\leq$60s of mechanical deformation while Chen et al. (2010), Pender & McCulloch (1991), and Krishnan et al. (2009) showed that upon release of the substrate the traction forces drop quickly but recover within few minutes. The 2-minute delays between the stretch intervals in our experiment could have given the recovery time to the stress fibers to rearrange and reinforce, and therefore, with the next intervals the reinforcement canceled out the substrate compression and we recorded similar traction forces. Similarly, Rosowski et al. (2018) showed that after the immediate increase of the traction forces due to a static stretch, the forces drop slowly indicating the cell's tendency to retract and rearrange in response to lasting stretch which can also explain the lower increase in the traction forces along the stretch axis compared to the sudden stretch. In line with this argument, are the changes in the cell areas observed during this experiment. Looking at the results, we can see that while almost all of the cells expanded in the sudden stretch experiment, the size of cell expansion in the gradual stretch experiment was smaller, and the number of cells that had partial detachment from the substrate instead of expanding was increased.

hAELVi$^{cav-/-}$ cells response to 50% strain

In contrast to the wild type cells, the total traction forces of the Cav1 knockout cells and the forces in the direction of the stress both dropped significantly in response to

the sudden stretch to 50% strain. The transverse forces also dropped as was expected due to the same reasons in the previous experiment. Gavara et al. (2008) suggested that despite the common belief that cell pre-stress provides a protective mechanism for it to preserve the structural integrity against the external stresses, its role could be reversed. It means that for a cell with a larger pre-stress, instead of a larger resistance to the strain (N. Wang et al., 1993), the larger pre-stress could bring the cytoskeleton closer to yield. Cirka et al. (2016) also concluded that the change of the traction forces as a response to the external stretch was dependent on the initial cell pre-stress; cytoskeletal tension at a maximal level reduces, whereas if below the maximal level, it increases toward the optimal level. Assuming that in the absence of caveolae hAELVi$^{cav-/-}$ cells are stiffer than the wild type cells, in addition to having a higher pre-stress, and while undergoing a large strain, Gavara et al. (2008) and Cirka et al. (2016) theory can explain the huge drop in the traction forces of the knockout cells. On the other hand, it is long believed that caveolae provide extra membrane that buffers the mechanical forces by rapid flattening and reducing the membrane tension passively (Dulhunty & Franzini-Armstrong, 1975; Sinha et al., 2011; Sens & Turner, 2006). Trepat et al. (2004) reported a partial cell detachment during the stretch and suggested that at high strain amplitudes cell adhesion could be compromised by stretch induced-stiffening. This is in line with our findings that the majority of knockout cells had partial detachment from the substrate. During the gradual stretch experiment, while the traction forces in the direction of stretch remained relatively unchanged, the transverse forces dropped significantly, and as the combination of both, the total traction forces showed an insignificant decrease. It is also notable that cells experiencing the gradual stretch had significantly smaller detachments. As discussed earlier, the rapid remodeling of the actin stress fibers can be associated with these results. Furthermore, Tondon & Kaunas (2014) showed that actin stress fibers in cells under cyclic stretch reoriented in the direction of stretch on low stiffness substrates. In the absence of caveolae (to provide membrane buffer) and cell stiffening with the sudden stretch, cells exhibited partial detachment, while the delays and the smaller stretch size in each interval in the gradual stretch seem to have given the knockout cells enough time to rearrange and reinforce the stress fibers which resulted in less cell detachment and improved traction forces. As for the transverse forces, the forces continued to reduce

with each interval which is different from what we saw from the wild type cells. This could emphasize the role of caveolae in mechanosensing and regulating the responses (Boyd et al., 2003; Park et al., 2000). As a possible reason, the cells might not have been able to sense the compression, or the lack of caveolae impaired their ability to deal with the buckling in the stress fibers, while being able to sens the stretch through other sensing components in the structure of the cell membrane and cytoskeleton.

Confluent cell layer with 10% strain

Showing the results of this experiment followed the simplified model of strain energy of a rectangle bar with the same size and mechanical characteristics as the gel layer stretched to 10% strain, proves that the calculation method is reliable. However, both empty and with confluent cell layer membranes created similar results that do not comply with the theory. The reason can be that cell layers show their mechanical properties at much higher than 10% strain (Harris et al., 2012). This was in line with traction forces of cells grown on a narrow strip where their CTF showed negligible change at 10% strain. For the strain energy calculation in our experiments, particle tracking was only possible at 0.5% strain per stretch step resulting in a 42 step stretch for only 10% strain, and continuing the experiment at higher strains was not feasible. Furthermore, to see the effect of a cell layer on the TFM substrate, a surrounding empty area is needed, and having a confluent cell layer on the whole gel area did not allow us to see this effect. As the preliminary results showed, a gel layer with a patterned coating small enough not to reach outside of the microscope field of view can overcome this problem. Furthermore, the experiment will be carried out more efficiently if conducted similarly to the experiments with single-cells, meaning each image will be compared to its equivalent image when cells are removed. This would eliminate the need for bead tracking with small steps, and the membrane can be stretched to any larger strains directly saving plenty of time without losing any beads in the tracking process.

4.2.3 Traction forces of cells under fluidic shear stress

Many studies have been carried out on cell motility under shear stress and with higher flow shear, for example, the shear stress of 4-12 dyn/cm^2 was applied to endothelial

cells in the study by Hur et al. (2012) which is much higher than 0.22-1.3dyn/cm^2 shear applied to ATI cells in our experiments. However, although the detachment of hAELVi^{wt} cells under low fluidic shear stress was not expected, alveolar cells are not the flow enduring cell types and are perhaps not the best for this kind of experiment. hAELVi cells in our experiment detached in less than 20 minutes even after the shear stress were removed.

On the other hand, there is a slight possibility that since the chamber was made before the gel was polymerized, this had affected the overall height of the chamber resulting in a higher flow rate than expected. This is less likely to have happened considering the chamber assembly process, and due to the thickness of the gel ($\sim$30 µm), the possible height change could not have caused a significant increase in the flow rate. A better alternative for this experiment is to monitor motility and the traction forces of ATI cells under static stretch (Buckley et al., 2001) and additionally speed up the migration by manipulating the coating concentration (Maheshwari et al., 1999).

4.3 Conclusion

The aim of this research was to fabricate a stretching platform equipped with traction force microscopy technique for real-time study of the alveolar epithelium and in particular ATI cells. The change of alveolar traction forces in response to large uniaxial deformation was recorded. The results of this work supported some of the previous hypotheses about mechanically-induced changes in the cytoskeleton reorientation and generation of traction forces. We showed that mutated alveolar cells lacking Cav1 are stiffer and have higher contractile force than their wild type counterparts. Contractile forces during a static stretch are reduced in an exponential trend. It was observed that wild type hAELVi responded to a fast and large stretch with stiffening and with increasing the traction force while the mutated cells responded by reducing their traction forces substantially during the same stretch process. The results for two different stretching process indicate that the mechanical response of cells to external stimuli is a combination of their mechanical properties as a matter and their dynamic of signaling cascades as a living thing. When subjected to a fast mechanical cue, the initial

responses of cells were through their mechanical properties; as a matter undergoing a tensile force, the cells responded with their stiffness. While the less stiff cells were able to undergo large strains the stiffer cells reached their yield and partially detached from the underlying substrate. However, when the cells were put through a slower stretching process we observed different responses created by the complex sensing structures and signaling pathways of the cells that can potentially affect the mechanical properties of a cell as well. Our results showed and confirmed the important role of caveolae in the structure of the alveolar cells, participating in both the mechanical properties and physiology of the alveolar cells. Indeed, there were some technical difficulties and limitations affecting the experiments and results, which can be eliminated with a few modifications in the setup and experiment process. In the case of further experiments with cells under fluidic shear stress, lower shear stress requires using a different tubing and possibly a costume-made flow chamber. For the experiment with a confluent cell layer, with some changes in the way in which the images were analyzed and compared larger strains will be possible without being limited to small steps. Ideally, this should be done on a small area of the membrane rather than a full layer. For traction microscopy in general, using smaller size beads will provide more accuracy as well as a smoother surface for cells to adhere but in this work, there was a limitation due to the incompatibility of available beads with our microscope system.

Overall, the method proved to be reliable and practical with the potential to be used for biaxial experiments or simultaneously with other sub-cellular studies.

Chapter 5

Summary

Mechanical forces are an inseparable part of the human body as a biological system. Cells and tissues are subjected to various types of forces that could be from the environment on the tissue/cells or generated within the cells by the cytoskeleton and exerted on the extracellular matrix (ECM). As these forces play a significant role in regulating developmental, physiological, and pathological processes, it is of great importance to understand how the cells sense these forces (mechanosensing) and translate them into biochemical signals (mechanotransduction). The lung is an organ that experiences cyclic mechanical forces by breathing such as the stretch on alveolar cells at the air-blood gas exchanging barrier; alveolar type I and type II epithelial cells (ATI and ATII). While the cuboidal ATII cells are mainly responsible to reduce the surface tension of the alveolus by secreting surfactant proteins, the squamous ATI cells contribute to the majority of the alveolar surface and undergo the mechanical stretch. ATI cells have plenty invaginations in their plasma membrane known as caveolae, which are believed to have a mechanosensing role. Caveolae are also associated with stress fibers that as part of the cytoskeleton contribute to cell contractile force generation. Measurement of contractile forces is one of the main topics of interest in research in understanding the sub-cellular pathways. These forces, however, are not directly measurable and are evaluated by the traction forces that the cell exerts on the underlying matrix or substrate, also known as cell traction forces. Traction force microscopy (TFM) is the technique that is used to measure cell traction forces. In this work, we tried to recreate the TFM

technique on an elastic substrate to study the alveolar traction forces under uniaxial stretch.

The elastic substrate was made in the form of a thin sheet/membrane consisting of two different layers of biocompatible polydimethylsiloxane (PDMS) polymer. The bottom layer was made of a stiffer type of PDMS to provide support for the top layer that was made of a much softer gel of PDMS during the stretch. This softer layer was added as the main requirement for the TFM technique. TFM measures the traction forces by measuring the deformation of the soft substrate by the adherent cell. To Produce these two layers we used spin coating to ensure the uniform thickness throughout the elastic sheet, which is a necessity for the microscopy and the force calculation. In order to quantify the substrate deformation, we added fluorescent beads on the surface of the softer layer, and we also added fluorescent beads at the bottom (between the soft and stiff polymer layers) to facilitate the exact measurement of the soft layer thickness during the stretch. With the help of Matlab codes in solving the theory of elasticity equations, the substrate deformation was measured and cell traction forces were calculated. For this research, we plated human alveolar epithelial lentivirus immortalized (hAELVi) cells, an ATI-like cell line, on these elastic membranes. We also used mutant hAELVi cells lacking caveolae to study their contribution to cell forces.

Our results showed that ATI cells produced less traction force than the caveolae deficient cells. In addition, the normal alveolar cells responded to the stretch of 50% strain magnitude by increasing their traction force. In contrast, the mutant cells lacking caveolae responded to the stretch differently, by reducing their traction force. The results of stretching the cells gradually, but to the same final strain magnitude of 50%, showed slight differences that indicated that the mechanical properties of the cells together with their physiology affect the cell response to mechanical cues where the duration of these cues also affect the cell responses.

In conclusion, our findings indicate that the mechanical response of alveolar cells to substrate stretch relies on both their physical properties and the signaling pathways triggered by the stretch and that caveolae potentially contribute to the force generation in response to the stretch. Our platform not only showed reliability for cell force measurements under mechanical stretch but also can be used for other investigations rather than single-cell studies provided proper modifications are applied.

References

Asmani, M., Kotei, C., Hsia, I., Marecki, L., Wang, T., Zhou, C., & Zhao, R. (2019). Cyclic stretching of fibrotic microtissue array for evaluation of anti-fibrosis drugs. *Cellular and molecular bioengineering*, *12*(5), 529–540. doi: 10.1007/s12195-019-00590-3

Balaban, N., Schwarz, U., Riveline, D., Goichberg, P., Tzur, G., Sabanay, I., ... Geiger, B. (2001). Force and focal adhesion assembly: a close relationship studied using elastic micropatterned substrates. *Nature Cell Biology*, *3*, 466-472.

Balaban, N. Q., Schwarz, U. S., Riveline, D., Goichberg, P., Tzur, G., Sabanay, I., ... Geige, B. (2001). Force and focal adhesion assembly: a close relationship studied using elastic micropatterned substrates. *Nature Cell Biology*, *3*, 466–472. Retrieved from `https://www.nature.com/articles/ncb0501_466` doi: https://doi.org/10.1038/35074532

Beningo, K. A., Hamao, K., Dembo, M., Wang, Y.-l., & Hosoya, H. (2006). Traction forces of fibroblasts are regulated by the rho-dependent kinase but not by the myosin light chain kinase. *Archives of Biochemistry and Biophysics*, *456*(2), 224-231. Retrieved from `https://www.sciencedirect.com/science/article/pii/S0003986106003699` doi: 10.1016/j.abb.2006.09.025

Boyd, N. L., Park, H., Yi, H., Boo, Y. C., Sorescu, G. P., Sykes, M., & Jo, H. (2003). Chronic shear induces caveolae formation and alters erk and akt responses in endothelial cells. *American Journal of Physiology-Heart and Circulatory Physiology*, *285*(3), H1113-H1122. Retrieved from `https://doi.org/10.1152/ajpheart.00302.2003` doi: 10.1152/ajpheart.00302.2003

Buckley, S., Driscoll, B., Shi, W., Anderson, K., & Warburton, D. (2001). Migration and gelatinases in cultured fetal, adult, and hyperoxic alveolar epithelial cells. *American Journal of Physiology-Lung Cellular and Molecular Physiology*, *281*(2), L427-L434. Retrieved from `https://doi.org/10.1152/ajplung.2001.281.2.L427` doi: 10.1152/ajplung.2001.281.2.L427

Burridge, K., & Wittchen, E. S. (2013). The tension mounts: Stress fibers as force-generating mechanotransducers. *Journal of Cell Biology*, *200*(1), 9-19. doi: 10.1083/jcb.201210090

Butler, J. P., Tolić-Nørrelykke, I. M., Fabry, B., & Fredberg, J. J. (2002). Traction fields, moments, and strain energy that cells exert on their surroundings. *American Journal of Physiology-Cell Physiology*, *282*(3), C595-C605. Retrieved from `https://doi.org/10.1152/ajpcell.00270.2001` doi: 10.1152/ajpcell.00270.2001

Buwa, N., Mazumdar, D., & Balasubramanian, N. (2020). Caveolin1 tyrosine-14 phosphorylation: Role in cellular responsiveness to mechanical cues. *The Journal of Membrane Biology*, *253*(6), 509-534. Retrieved from `https://doi.org/10.1007/s00232-020-00143-0` doi: 10.1007/s00232-020-00143-0

Chen, C., Krishnan, R., Zhou, E., Ramachandran, A., Tambe, D., Rajendran, K., ... Fredberg, J. J. (2010). Fluidization and resolidification of the human bladder smooth muscle cell in response to transient stretch. *PloS one*, *5*(8), e12035. doi: 10.1371/journal.pone.0012035

Chiu, W.-T., Wang, Y.-H., Tang, M.-J., & Shen, M.-R. (2007). Soft substrate induces apoptosis by the disturbance of ca2+ homeostasis in renal epithelial llc-pk1 cells. *Journal of Cellular Physiology*, *212*(2), 401-410. Retrieved from `https://onlinelibrary.wiley.com/doi/abs/10.1002/jcp.21037` doi: https://doi.org/10.1002/jcp.21037

Cirka, H., Monterosso, M., Diamantides, N., Favreau, J., Wen, Q., & Billiar, K. (2016). Active traction force response to long-term cyclic stretch is dependent on cell prestress. *Biophysical journal*, *110*(8), 1845-1857. doi: 10.1016/j.bpj.2016.02.036

Cohen, T. S., Cavanaugh, K. J., & Margulies, S. S. (2008). Frequency and peak stretch magnitude affect alveolar epithelial permeability. *European Respiratory Journal*, *32*(4), 854–861. Retrieved from https://erj.ersjournals.com/content/32/4/854 doi: 10.1183/09031936.00141007

Costa, K. D., Hucker, W. J., & Yin, F. C. P. (2002). Buckling of actin stress fibers: A new wrinkle in the cytoskeletal tapestry. *Cell Motility*, *52*(4), 266-274. Retrieved from https://onlinelibrary.wiley.com/doi/abs/10.1002/cm.10056 doi: 10.1002/cm.10056

Diem, K., Fauler, M., Fois, G., Hellmann, A., Winokurow, N., Schumacher, S., ... Frick, M. (2020). Mechanical stretch activates piezo1 in caveolae of alveolar type i cells to trigger atp release and paracrine stimulation of surfactant secretion from alveolar type ii cells. *The FASEB Journal*, *34*(9), 12785-12804. Retrieved from https://faseb.onlinelibrary.wiley.com/doi/abs/10.1096/fj.202000613RRR doi: 10.1096/fj.202000613RRR

Discher, D. E., Janmey, P., & Wang, Y.-l. (2005). Tissue cells feel and respond to the stiffness of their substrate. *Science*, *310*(5751), 1139-1143. Retrieved from https://science.sciencemag.org/content/310/5751/1139 doi: 10.1126/science.1116995

Drab, M., Verkade, P., Elger, M., Kasper, M., Lohn, M., Lauterbach, B., ... Kurzchalia, T. V. (2001). Loss of caveolae, vascular dysfunction, and pulmonary defects in caveolin-1 gene-disrupted mice. *Science*, *293*(5539), 2449–2452. Retrieved from https://science.sciencemag.org/content/293/5539/2449 doi: 10.1126/science.1062688

Dulhunty, A. F., & Franzini-Armstrong, C. (1975). The relative contributions of the folds and caveolae to the surface membrane of frog skeletal muscle fibres at different sarcomere lengths. *The Journal of Physiology*, *250*(3), 513-539. Retrieved from https://physoc.onlinelibrary.wiley.com/doi/abs/10.1113/jphysiol.1975.sp011068 doi: https://doi.org/10.1113/jphysiol.1975.sp011068

Echarri, A., & Del Pozo, M. A. (2015). Caveolae - mechanosensitive membrane invaginations linked to actin filaments. *Journal of cell science*, *128*(15), 2747-2758. doi: doi:10.1242/jcs.153940

Edwards, Y. S. (2001). Stretch stimulation: its effects on alveolar type ii cell function in the lung. *Comparative Biochemistry and Physiology Part A: Molecular & Integrative Physiology*, *129*(1), 245-260. Retrieved from `https://www.sciencedirect.com/science/article/pii/S109564330100321X` (Surfactant, Lungs and the Evolution of Air Breathing - Tribute to R.E. Pattle) doi: 10.1016/S1095-6433(01)00321-X

Engler, A. J., Sen, S., Sweeney, H. L., & Discher, D. E. (2006). Matrix elasticity directs stem cell lineage specification. *Cell*, *126*(4), 677-689. Retrieved from `https://doi.org/10.1016/j.cell.2006.06.044` doi: 10.1016/j.cell.2006.06.044

Foster, C. D., Varghese, L. S., Gonzales, L. W., Margulies, S. S., & Guttentag, S. H. (2010). The rho pathway mediates transition to an alveolar type i cell phenotype during static stretch of alveolar type ii cells. *Pediatric research*, *67*(6), 585–590. doi: 10.1203/PDR.0b013e3181dbc708

Frank, P. G., Woodman, S. E., Park, D. S., & Lisanti, M. P. (2003). Caveolin, caveolae, and endothelial cell function. *Arteriosclerosis, Thrombosis, and Vascular Biology*, *23*(7), 1161-1168. doi: 10.1161/01.ATV.0000070546.16946.3A

Gavara, N., Roca-Cusachs, P., Sunyer, R., Farré, R., & Navajas, D. (2008). Mapping cell-matrix stresses during stretch reveals inelastic reorganization of the cytoskeleton. *Biophysical journal*, *95*(1), 464–471. doi: 10.1529/biophysj.107.124180

Geiger, B., Spatz, J. P., & Bershadsky, A. D. (2009). Environmental sensing through focal adhesions. *Nature Reviews Molecular Cell Biology*, *10*(1), 21–33. doi: https://doi.org/10.1038/nrm2593

Gerstmair, A., Fois, G., Innerbichler, S., Dietl, P., & Felder, E. (2009). A device for simultaneous live cell imaging during uni-axial mechanical strain or compression. *Journal of Applied Physiology*, *107*(2), 613-620. Retrieved from `https://doi.org/10.1152/japplphysiol.00012.2009` doi: 10.1152/japplphysiol.00012.2009

Gilbert, G., Ducret, T., Savineau, J.-P., Marthan, R., & Quignard, J.-F. (2016). Caveolae are involved in mechanotransduction during pulmonary hypertension. *American Journal of Physiology-Lung Cellular and Molecular Physiology*, *310*(11), L1078-L1087. Retrieved from https://doi.org/10.1152/ajplung.00198.2015 doi: 10.1152/ajplung.00198.2015

Goffin, J. M., Pittet, P., Csucs, G., Lussi, J. W., Meister, J.-J., & Hinz, B. (2006). Focal adhesion size controls tension-dependent recruitment of α-smooth muscle actin to stress fibers. *Journal of Cell Biology*, *172*(2), 259-268. Retrieved from https://doi.org/10.1083/jcb.200506179 doi: 10.1083/jcb.200506179

Grinnell, F., Zhu, M., Carlson, M. A., & Abrams, J. M. (1999). Release of mechanical tension triggers apoptosis of human fibroblasts in a model of regressing granulation tissue. *Experimental Cell Research*, *248*(2), 608-619. Retrieved from https://www.sciencedirect.com/science/article/pii/S0014482799944403 doi: https://doi.org/10.1006/excr.1999.4440

Grivas, D., González-Rajal, l., Rodríguez, C. G., Garcia, R., & de la Pompa, J. L. (2020). Loss of caveolin-1 and caveolae leads to increased cardiac cell stiffness and functional decline of the adult zebrafish heart. *Scientific Reports*, *10*. Retrieved from https://doi.org/10.1038/s41598-020-68802-9 doi: 10.1038/s41598-020-68802-9

Han, S. J., Bielawski, K. S., Ting, L. H., Rodriguez, M. L., & Sniadecki, N. J. (2012). Decoupling substrate stiffness, spread area, and micropost density: A close spatial relationship between traction forces and focal adhesions. *Biophysical Journal*, *103*(4), 640-648. Retrieved from http://www.sciencedirect.com/science/article/pii/S0006349512007989 doi: 10.1016/j.bpj.2012.07.023

Harris, A. R., Peter, L., Bellis, J., Baum, B., Kabla, A. J., & Charras, G. T. (2012). Characterizing the mechanics of cultured cell monolayers. *Proceedings of the National Academy of Sciences*, *109*(41), 16449-16454. Retrieved from https://www.pnas.org/content/109/41/16449 doi: 10.1073/pnas.1213301109

Hayakawa, K., Tatsumi, H., & Sokabe, M. (2012). Mechano-sensing by actin filaments and focal adhesion proteins. *Communicative & integrative biology*, *5*(6), 572-577. doi: 10.4161/cib.21891

Hur, S. S., del Álamo, J. C., Park, J. S., Li, Y.-S., Nguyen, H. A., Teng, D., ... Chien, S. (2012). Roles of cell confluency and fluid shear in 3-dimensional intracellular forces in endothelial cells. *Proceedings of the National Academy of Sciences*, *109*(28), 11110-11115. Retrieved from `https://www.pnas.org/content/109/28/11110` doi: 10.1073/pnas.1207326109

Kaunas, R., Nguyen, P., Usami, S., & Chien, S. (2005). Cooperative effects of rho and mechanical stretch on stress fiber organization. *Proceedings of the National Academy of Sciences*, *102*(44), 15895-15900. Retrieved from `https://www.pnas.org/content/102/44/15895` doi: 10.1073/pnas.0506041102

Kee, Y.-S., & Robinson, D. N. (2008). Motor proteins: Myosin mechanosensors. *Current Biology*, *18*(18), R860-R862. Retrieved from `http://www.sciencedirect.com/science/article/pii/S0960982208010166` doi: 10.1016/j.cub.2008.07.071

Koch, T. M., Münster, S., Bonakdar, N., Butler, J. P., & Fabry, B. (2012). 3d traction forces in cancer cell invasion. *PLOS ONE*, *7*(3), 1-8. Retrieved from `https://doi.org/10.1371/journal.pone.0033476` doi: 10.1371/journal.pone.0033476

Krishnan, R., Park, C. Y., Lin, Y.-C., Mead, J., Jaspers, R. T., Trepat, X., ... Fredberg, J. J. (2009). Reinforcement versus fluidization in cytoskeletal mechanoresponsiveness. *PloS one*, *4*(5), e5486. doi: 10.1371/journal.pone.0005486

Kuehn, A., Kletting, S., de Souza Carvalho-Wodarz, C., Repnik, U., Griffiths, G., Fischer, U., ... Lehr, C.-M. (2016). Human alveolar epithelial cells expressing tight junctions to model the air-blood barrier. *ALTEX - Alternatives to Animal Experimentation*, *33*(3), 251-260. Retrieved from `https://doi.org/10.14573/altex.1511131` doi: 10.14573/altex.1511131

Laakso, J. M., Lewis, J. H., Shuman, H., & Ostap, E. M. (2008). Myosin i can act as a molecular force sensor. *Science*, *321*(5885), 133-136. Retrieved from `https://science.sciencemag.org/content/321/5885/133` doi: 10.1126/science.1159419

Lam, R. H. W., Weng, S., Lu, W., & Fu, J. (2012). Live-cell subcellular measurement of cell stiffness using a microengineered stretchable micropost array membrane. *Integrative Biology*, *4*(10), 1289-1298. Retrieved from https://doi.org/10.1039/c2ib20134h doi: 10.1039/c2ib20134h

Lambert, C., Soudant, E., Nusgens, B., & Lapière, C. (1992). Pretranslational regulation of extracellular matrix macromolecules and collagenase expression in fibroblasts by mechanical forces. *Laboratory investigation; a journal of technical methods and pathology*, *66*(4), 444—451. Retrieved from http://europepmc.org/abstract/MED/1316527

Landau, L. D., & Lifshitz, E. M. (1982). *Mechanics* (3rd ed., Vol. 1). Oxford: Pergamon Press.

Landau, L. D., & Lifshitz, E. M. (1984). *Theory of elasticity* (3rd ed., Vol. 7). Oxford: Pergamon Press.

Li, Y.-S. J., Haga, J. H., & Chien, S. (2005). Molecular basis of the effects of shear stress on vascular endothelial cells. *Journal of Biomechanics*, *38*(10), 1949-1971. Retrieved from https://www.sciencedirect.com/science/article/pii/S0021929004004580 doi: https://doi.org/10.1016/j.jbiomech.2004.09.030

Liu, M., & Post, M. (2000). Invited review: Mechanochemical signal transduction in the fetal lung. *Journal of Applied Physiology*, *89*(5), 2078-2084. Retrieved from https://doi.org/10.1152/jappl.2000.89.5.2078 doi: 10.1152/jappl.2000.89.5.2078

Liu, M., Skinner, S. J., Xu, J., Han, R. N., Tanswell, A. K., & Post, M. (1992). Stimulation of fetal rat lung cell proliferation in vitro by mechanical stretch. *American Journal of Physiology-Lung Cellular and Molecular Physiology*, *263*(3), L376-L383. Retrieved from https://doi.org/10.1152/ajplung.1992.263.3.L376 doi: 10.1152/ajplung.1992.263.3.L376

Lo, C.-M., Wang, H.-B., Dembo, M., & Wang, Y.-l. (2000). Cell movement is guided by the rigidity of the substrate. *Biophysical Journal*, *79*(1), 144-152. Re-

trieved from https://doi.org/10.1016/S0006-3495(00)76279-5 doi: 10.1016/S0006-3495(00)76279-5

Maheshwari, G., Wells, A., Griffith, L. G., & Lauffenburger, D. A. (1999). Biophysical integration of effects of epidermal growth factor and fibronectin on fibroblast migration. *Biophysical Journal*, *76*(5), 2814 - 2823. Retrieved from http://www.sciencedirect.com/science/article/pii/S0006349599774357 doi: https://doi.org/10.1016/S0006-3495(99)77435-7

Mann, J. M., Lam, R. H. W., Weng, S., Sun, Y., & Fu, J. (2012). A silicone-based stretchable micropost array membrane for monitoring live-cell subcellular cytoskeletal response. *Lab on a chip*, *12*(4), 731–740. doi: 10.1039/c2lc20896b

Martinac, B. (2004). Mechanosensitive ion channels: molecules of mechanotransduction. *Journal of Cell Science*, *117*(12), 2449-2460. Retrieved from https://jcs.biologists.org/content/117/12/2449 doi: 10.1242/jcs.01232

Maskarinec, S. A., Franck, C., Tirrell, D. A., & Ravichandran, G. (2009). Quantifying cellular traction forces in three dimensions. *Proceedings of the National Academy of Sciences*, *106*(52), 22108-22113. Retrieved from https://www.pnas.org/content/106/52/22108 doi: 10.1073/pnas.0904565106

Moreno-Vicente, R., Pavón, D. M., Inés Martín-Padura, I., Català-Montoro, M., Díez-Sánchez, A., Quílez-Álvarez, A., ... Del Pozo, M. A. (2018). Caveolin-1 modulates mechanotransduction responses to substrate stiffness through actin-dependent control of yap. *Cell reports*, *25*(6), 1622–1635.e6. Retrieved from https://www.ncbi.nlm.nih.gov/pmc/articles/PMC6231326/ doi: 10.1016/j.celrep.2018.10.024

Nova, Z., Skovierova, H., & Calkovska, A. (2019). Alveolar-capillary membrane-related pulmonary cells as a target in endotoxin-induced acute lung injury. *International Journal of Molecular Sciences*, *20*(4). Retrieved from https://www.mdpi.com/1422-0067/20/4/831 doi: 10.3390/ijms20040831

Palchesko, R. N., Zhang, L., Sun, Y., & Feinberg, A. W. (2012). Development of polydimethylsiloxane substrates with tunable elastic modulus to study cell mechanobi-

ology in muscle and nerve. *PLOS ONE*, *7*(12), 1-13. Retrieved from https://doi.org/10.1371/journal.pone.0051499 doi: 10.1371/journal.pone.0051499

Park, H., Go, Y.-M., Darji, R., Choi, J.-W., Lisanti, M. P., Maland, M. C., & Jo, H. (2000). Caveolin-1 regulates shear stress-dependent activation of extracellular signal-regulated kinase. *American Journal of Physiology-Heart and Circulatory Physiology*, *278*(4), H1285-H1293. Retrieved from https://doi.org/10.1152/ajpheart.2000.278.4.H1285 doi: 10.1152/ajpheart.2000.278.4.H1285

Pender, N., & McCulloch, C. (1991). Quantitation of actin polymerization in two human fibroblast sub-types responding to mechanical stretching. *Journal of Cell Science*, *100*(1), 187-193. Retrieved from https://jcs.biologists.org/content/100/1/187

Puchner, E. M., Alexandrovich, A., Kho, A. L., Hensen, U., Schäfer, L. V., Brandmeier, B., ... Gautel, M. (2008). Mechanoenzymatics of titin kinase. *Proceedings of the National Academy of Sciences*, *105*(36), 13385-13390. Retrieved from https://www.pnas.org/content/105/36/13385 doi: 10.1073/pnas.0805034105

Rausch, V., & Hansen, C. G. (2020). The hippo pathway, yap/taz, and the plasma membrane. *Trends in Cell Biology*, *30*(1), 32-48. Retrieved from https://www.sciencedirect.com/science/article/pii/S0962892419301680 doi: 10.1016/j.tcb.2019.10.005

Rogers, S. S., Waigh, T. A., Zhao, X., & Lu, J. R. (2007). Precise particle tracking against a complicated background: polynomial fitting with gaussian weight. *Physical Biology*, *4*(3), 220-227. Retrieved from https://doi.org/10.1088/1478-3975/4/3/008 doi: 10.1088/1478-3975/4/3/008

Rosowski, K. A., Boltyanskiy, R., Xiang, Y., Van den Dries, K., Schwartz, M. A., & Dufresne, E. R. (2018). Vinculin and the mechanical response of adherent fibroblasts to matrix deformation. *Scientific reports*, *8*(1), 17967. doi: 10.1038/s41598-018-36272-9

Rothberg, K. G., Heuser, J. E., Donzell, W. C., Ying, Y.-S., Glenney, J. R., & Anderson, R. G. (1992). Caveolin, a protein component of caveolae mem-

brane coats. *Cell*, *68*(4), 673-682. Retrieved from http://www.sciencedirect.com/science/article/pii/009286749290143Z doi: https://doi.org/10.1016/0092-8674(92)90143-Z

Sabass, B., Gardel, M. L., Waterman, C. M., & Schwarz, U. S. (2008). High resolution traction force microscopy based on experimental and computational advances. *Biophysical Journal*, *94*(1), 207-220. Retrieved from https://www.sciencedirect.com/science/article/pii/S000634950870780X doi: https://doi.org/10.1529/biophysj.107.113670

Sanchez-Esteban, J., Cicchiello, L. A., Wang, Y., Tsai, S.-W., Williams, L. K., Torday, J. S., & Rubin, L. P. (2001). Mechanical stretch promotes alveolar epithelial type ii cell differentiation. *Journal of Applied Physiology*, *91*(2), 589-595. Retrieved from https://doi.org/10.1152/jappl.2001.91.2.589 doi: 10.1152/jappl.2001.91.2.589

Schwarz, U. S., & Soiné, J. R. (2015). Traction force microscopy on soft elastic substrates: A guide to recent computational advances. *Biochimica et Biophysica Acta (BBA) - Molecular Cell Research*, *1853*(11, Part B), 3095-3104. Retrieved from http://www.sciencedirect.com/science/article/pii/S0167488915001822 doi: 10.1016/j.bbamcr.2015.05.028

Sens, P., & Turner, M. S. (2006). Budded membrane microdomains as tension regulators. *Phys. Rev. E*, *73*, 031918. Retrieved from https://link.aps.org/doi/10.1103/PhysRevE.73.031918 doi: 10.1103/PhysRevE.73.031918

Shyy, J. Y.-J., & Chien, S. (2002). Role of integrins in endothelial mechanosensing of shear stress. *Circulation Research*, *91*(9), 769-775. Retrieved from https://www.ahajournals.org/doi/abs/10.1161/01.RES.0000038487.19924.18 doi: 10.1161/01.RES.0000038487.19924.18

Sinha, B., Köster, D., Ruez, R., Gonnord, P., Bastiani, M., Abankwa, D., ... Nassoy, P. (2011). Cells respond to mechanical stress by rapid disassembly of caveolae. *Cell*, *144*(3), 402-413. Retrieved from http://www.sciencedirect.com/science/article/pii/S0092867410015230 doi: 10.1016/j.cell.2010.12.031

Stahlhut, M., & van Deurs, B. (2000). Identification of filamin as a novel ligand for caveolin-1: Evidence for the organization of caveolin-1–associated membrane domains by the actin cytoskeleton. *Molecular Biology of the Cell*, *11*(1), 325-337. Retrieved from https://doi.org/10.1091/mbc.11.1.325 doi: 10.1091/mbc.11.1.325

Style, R. W., Boltyanskiy, R., German, G. K., Hyland, C., MacMinn, C. W., Mertz, A. F., ... Dufresne, E. R. (2014). Traction force microscopy in physics and biology. *Soft Matter*, *10*, 4047-4055. doi: 10.1039/C4SM00264D

Suki, B., Ito, S., Stamenović, D., Lutchen, K. R., & Ingenito, E. P. (2005). Biomechanics of the lung parenchyma: critical roles of collagen and mechanical forces. *Journal of Applied Physiology*, *98*(5), 1892-1899. Retrieved from https://doi.org/10.1152/japplphysiol.01087.2004 doi: 10.1152/japplphysiol.01087.2004

Thévenaz, P., Ruttimann, U. E., & Unser, M. (1998). A pyramid approach to subpixel registration based on intensity. *IEEE Transactions on Image Processing*, *7*(1), 2741.

Tondon, A., & Kaunas, R. (2014). The direction of stretch-induced cell and stress fiber orientation depends on collagen matrix stress. *PLOS ONE*, *9*(2), 1-10. Retrieved from https://doi.org/10.1371/journal.pone.0089592 doi: 10.1371/journal.pone.0089592

Torday, J. S., Sanchez-Esteban, J., & Rubin, L. (1998). Paracrine mediators of mechanotransduction in lung development. *The American Journal of the Medical Sciences*, *316*(3), 205-208. Retrieved from https://www.sciencedirect.com/science/article/pii/S0002962915404033 doi: 10.1016/S0002-9629(15)40403-3

Trepat, X., Deng, L., An, S. S., Navajas, D., Tschumperlin, D. J., Gerthoffer, W. T., ... Fredberg, J. J. (2007). Universal physical responses to stretch in the living cell. *Nature*, *447*, 592-595. doi: 10.1038/nature05824

Trepat, X., Grabulosa, M., Puig, F., Maksym, G. N., Navajas, D., & Farré, R. (2004). Viscoelasticity of human alveolar epithelial cells subjected to stretch. *American Journal of Physiology-Lung Cellular and Molecular Physiology*, *287*(5), L1025-L1034. doi: 10.1152/ajplung.00077.2004

Tseng, Q., Duchemin-Pelletier, E., Deshiere, A., Balland, M., Guillou, H., Filhol, O., & Théry, M. (2012). Spatial organization of the extracellular matrix regulates cell–cell junction positioning. *Proceedings of the National Academy of Sciences*. Retrieved from https://www.pnas.org/content/early/2012/01/09/1106377109 doi: 10.1073/pnas.1106377109

Vogel, V., & Sheetz, M. (2006). Local force and geometry sensing regulate cell functions. *Nature Reviews Molecular Cell Biology*, *7*(4), 265-275. Retrieved from https://doi.org/10.1038/nrm1890 doi: 10.1038/nrm1890

Wang, J. H.-C., & Lin, J.-S. (2007). Cell traction force and measurement methods. *Biomechanics and modeling in mechanobiology*, *6*(6), 361—371. Retrieved from https://doi.org/10.1007/s10237-006-0068-4 doi: 10.1007/s10237-006-0068-4

Wang, N., Butler, J. P., & Ingber, D. E. (1993). Mechanotransduction across the cell surface and through the cytoskeleton. *Science*, *260*(5111), 1124-1127. Retrieved from https://science.sciencemag.org/content/260/5111/1124 doi: 10.1126/science.7684161

Wang, N., Tolić-Nørrelykke, I. M., Chen, J., Mijailovich, S. M., Butler, J. P., Fredberg, J. J., & Stamenović, D. (2002). Cell prestress. i. stiffness and prestress are closely associated in adherent contractile cells. *American Journal of Physiology-Cell Physiology*, *282*(3), C606-C616. doi: 10.1152/ajpcell.00269.2001

Wang, Y.-L., & Pelham, R. J. (1998). [39] preparation of a flexible, porous polyacrylamide substrate for mechanical studies of cultured cells. In (Vol. 298, p. 489-496). Academic Press. Retrieved from https://www.sciencedirect.com/science/article/pii/S0076687998980417 doi: https://doi.org/10.1016/S0076-6879(98)98041-7

Yonemura, S., Wada, Y., Watanabe, T., Nagafuchi, A., & Shibata, M. (2010). α-catenin as a tension transducer that induces adherens junction development. *Nature Cell Biology*, *12*(6), 533-542. Retrieved from https://doi.org/10.1038/ncb2055 doi: 10.1038/ncb2055

Appendix A

Gel thickness calculation

The value of Poisson's ratio by definition is the ratio of transverse strain to axial strain. For a cube of an isotropic and linearly elastic material with side length L stretched in the direction x:

$$\nu \approx -\frac{\Delta L'}{\Delta L}$$

ν: Poisson's ratio,

ΔL: axial elongation,

$\Delta L'$: transverse compression,

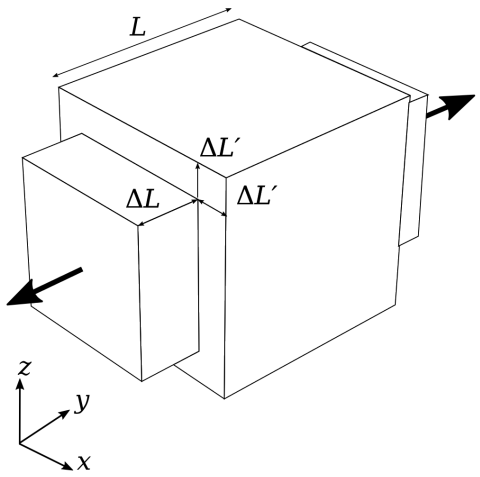

Figure A.1

Poisson's ratio for an incompressible material is 0.5, so for a given stretch with strain ε, the new length of the cube in the transverse direction can be calculated using

$\Delta L' = -\Delta L\nu = -0.5\,\Delta L,\ \varepsilon = \frac{\Delta L}{L}$

$\Delta L' = L_{y,z} - L = -0.5\,L\,\varepsilon$

$\Rightarrow L_{y,z} = L(1 - 0.5\,\varepsilon),\ \varepsilon' = \frac{\Delta L'}{L}$

with $L_{y,z}$ being the compressed length and ε' as the compression strain in the transverse directions. Taking L as the gel thickness before the stretch, for strains of 20%, 35%, and 50% the gel thickness and the compression strains are:

$$\varepsilon = 0.2 \Rightarrow \qquad L_z = 0.9\,L, \qquad \varepsilon' = -10\%$$
$$\varepsilon = 0.35 \Rightarrow \qquad L_z = 0.825\,L, \qquad \varepsilon' = -17.5\%$$
$$\varepsilon = 0.50 \Rightarrow \qquad L_z = 0.75\,L, \qquad \varepsilon' = -25\%$$

Gel layer thickness [µm]			
0%	20%	35%	50%
62	55.8	51.2	46.5
61	54.9	50.3	45.8
60	54.0	49.5	45.0
59	53.1	48.7	44.3
58	52.2	47.9	43.5
57	51.3	47.0	42.8
56	50.4	46.2	42.0
55	49.5	45.4	41.3
54	48.6	44.6	40.5

Appendix B

Additional codes

The TFM Matlab code and the Poly-particle tracker code are two independent programs. The following commands are added to the main TFM code to run the Poly-particle tracker within this program and to extract and convert the outputs accordingly. First, the Poly-particle tracker is moved as a sub-folder to the TFM code folder under the path $Users\backslash Susan\backslash Documents\backslash MATLAB\backslash TFMmulti$. Additional parameters required by the TFM code are the pixel size and the gel thickness in meter, and Young's modulus in pascal units. These values could be manually entered but to make the usage easier and avoid typos and mistakes in conversion they are added at the beginning of the TFM code:

```
pix=input('\n Size of pixel in Nanometers: ')*10^-9;
EM=input('\n Young''s modulus in Kilo Pascal: ')*10^3;
thick=input('\n Film thickness in Micron: ')*10^-6;
```

The PolyParticleTracker GUI is called up by the following command:
data = polyparticletracker_gui;
The window is brought up with default settings that do not need to be changed if the images are of good quality and the particles are round. In the field for filename add the file path with its name without a number: "path/image" and the first image in the sequence that is named image1, image2, ... will be shown in the box. Set the maximum track length at the bottom to the total number of frames you want to track. If the number is bigger than the number of available frames, the code will crash.

Important note: the codes here are written with the consideration that the control image is the first image with number 1.
For simple TFM two images are required, and in the case of flow experiments where there are multiple frames:

```
NFrames=length(data.mmov);
```

Additional presets to keep the sidebar of stress images identical for all frames, otherwise, the sidebar will be set differently depending on the maximum stress measured in each frame.

```
TFM.raw(NFrames+1).sed_max=0;
TFM.raw(NFrames+1).eachmax=0;
TFM.gaus(NFrames+1).eachmax=0;
```

The output **data** is created as a structure containing the following fields:
tr: a cell array containing the track and measurements for each particle.
tr_lst: an array with all identified particles in all frames.
mmov: Matlab-format movie of tracked particles with background image.



Figure B.1: Structures **d** and **data**. If you manually transfer data to d, note that all four arrays must have the same n×2 dimension.

The displacement field needed for the TFM code is a structure named **d** containing two fields:
r: the position of beads.
dr: the distance of each bead from its reference point.
Here the reference point is d(1).r meaning that d(1).dr will be zero and d(2).dr is the displacement data created by subtracting d(1).r from d(2).r, but depending on what we want to do this could be the positions of the beads in the first frame or the last frame.

Each row in this array indicates one specific bead while each column in data.tr indicates a bead and each row inside each cell is the position of the same bead in each frame. Transferring the tracking results of *data* into *d* structure:

```
for k=1: NFrames % This loop ends at the end of all calculations
  for i=1: length (data.tr)
        d(1).r(i,1)=data.tr{1, i}(1,1);
        d(1).r(i,2)=data.tr{1, i}(1,2);
        d(2).r(i,1)=data.tr{1, i}(k,1);
        d(2).r(i,2)=data.tr{1, i}(k,2);

        d(1).dr(i,1)=0;
        d(1).dr(i,2)=0;
        d(2).dr(i,1)=d(2).r(i,1)-d(1).r(i,1);
        d(2).dr(i,2)=d(2).r(i,2)-d(1).r(i,2);
  end;
```

Values are in pixel and must be converted to units of length before stresses are calculated:

```
  for i=1:length(d(1).r)
        d(1).r(i,1)=d(1).r(i,1)*pix;
        d(1).r(i,2)=d(1).r(i,2)*pix;
        d(2).r(i,1)=d(2).r(i,1)*pix;
        d(2).r(i,2)=d(2).r(i,2)*pix;

        d(2).dr(i,1)=d(2).dr(i,1)*pix;
        d(2).dr(i,2)=d(2).dr(i,2)*pix;
  end;
```

Once the TFM code runs, additional calculations will be saved in structure D. For separation of stresses in X and Y directions, SED calculations, and additional images we need to save these data for each frame before they're overwritten in each loop. Structure **TFM** with two fields **raw** and **gaus** are created to store all these information

for each frame:

```
TFM.raw(k).r=d(2).r;
TFM.raw(k).dr=d(2).dr;
TFM.raw(k).dx_interp=d(2).dx_interp;
TFM.raw(k).dy_interp=d(2).dy_interp;
TFM.raw(k).fov=d(2).fov;
TFM.raw(k).stress_x=d(2).stress_x;
TFM.raw(k).stress_y=d(2).stress_y;
TFM.raw(k).ux=d(2).ux;
TFM.raw(k).uy=d(2).uy;
TFM.raw(k).sed=d(2).sed;
TFM.raw(k).sed_sum=sum(sum(d(2).sed));
TFM.raw(k).eachframe=sqrt(((d(2).stress_x.*d(2).fov).^2)+
                          ((d(2).stress_y.*d(2).fov).^2));
TFM.raw(k).eachmax= max(max(TFM.raw(k).eachframe));
TFM.raw(k).sed_max=max(max(TFM.raw(k).sed));
```

Keeping the maximum stress value for use in the sidebar of stress images:

```
TFM.raw(NFrames+1).eachmax=max(TFM.raw(k).eachmax,
                               TFM.raw(NFrames+1).eachmax);
TFM.raw(NFrames+1).sed_max=max(TFM.raw(k).sed_max,
                               TFM.raw(NFrames+1).sed_max);
```

Adding Gaussian Filter on Stress field:

```
FiltGaus=fspecial('gaussian');
TFM.gaus(k).eachframe=filter2(FiltGaus,TFM.raw(k).eachframe);
TFM.gaus(k).eachmax= max(max(TFM.gaus(k).eachframe));
```

Keeping the overall maximum for imaging, and ending the first loop:

```
TFM.gaus(NFrames+1).eachmax=max(TFM.gaus(k).eachmax,
                                TFM.gaus(NFrames+1).eachmax);
end; % End of the first loop with variable k
```

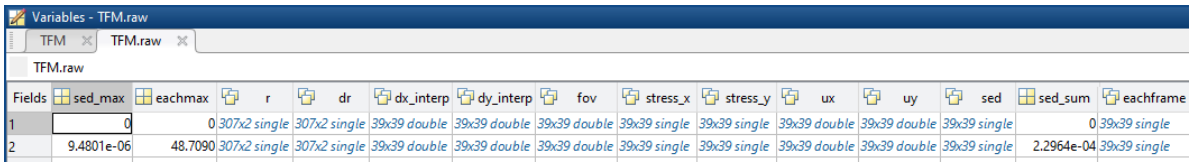

Fields	sed_max	eachmax	r	dr	dx_interp	dy_interp	fov	stress_x	stress_y	ux	uy	sed	sed_sum	eachframe
1	0	0	307x2 single	307x2 single	39x39 double	39x39 double	39x39 double	39x39 single	39x39 single	39x39 double	39x39 double	39x39 single	0	39x39 single
2	9.4801e-06	48.7090	307x2 single	307x2 single	39x39 double	39x39 double	39x39 double	39x39 single	39x39 single	39x39 double	39x39 double	39x39 single	2.2964e-04	39x39 single

Figure B.2: Cells inside the **TFM** structure containing different calculations such as displacement, stress, and surface energy density. Each cell is an n×n array with values referring to the same location on the live cell image with an n×n grid.

Saving all the calculations, variables, structures, etc. for later usage especially the particle tracking:

```
save('Entire evaluation');
```

Graphs for stresses in total, X, and Y directions:

```
barlim=[0 TFM.gaus(NFrames+1).eachmax];
h=figure;
imagesc(TFM.gaus(k).eachframe, barlim);  colorbar;
hold off
pause(.1)
xlabel('x [m]')
ylabel('y [m]')
title('Traction stress magnitude (Filtered) [Pa]')
saveas(h,sprintf('Traction plot%d.tiff',k));

barlim=[0 TFM.gaus(NFrames+1).eachmax];
h=figure;
imagesc(filter2(FiltGaus,abs(TFM.raw(k).stress_x.
                *TFM.raw(k).fov)), barlim);  colorbar;
hold off
pause(.1)
xlabel('x [m]')
ylabel('y [m]')
title('Traction stress magnitude X (Filtered) [Pa]')
saveas(h,sprintf('Traction plot_X%d.tiff',k));
```

```
barlim=[0 TFM.gaus(NFrames+1).eachmax];
h=figure;
imagesc(filter2(FiltGaus,abs(TFM.raw(k).stress_y.
                *TFM.raw(k).fov)), barlim);  colorbar;
hold off
pause(.1)
xlabel('x [m]')
ylabel('y [m]')
title('Traction stress magnitude Y (Filtered) [Pa]')
saveas(h,sprintf('Traction plot_Y%d.tiff',k));
```

Similarly separating the interpolation data in X and Y directions:

```
im=double(imread('live.tif'))/max(max(double(imread('live.tif'
                                                    ))));
h=figure;
imagesc(im); colormap gray
hold on
size_cell_image=size(im); % Size of control image in pixels
quiver(X/pix,Y/pix,TFM.raw(k).dx_interp/pix,0
        *TFM.raw(k).dy_interp/pix);
axis image
xlabel('x [pixels]');
ylabel('y [pixels]');
title('Map of interpolated X displacements')
axis([0 size_cell_image(2) 0 size_cell_image(1)]);
pause(0.1)
saveas(h,sprintf('interpolate_X%d.tiff',k));

im=double(imread('live.tif'))/max(max(double(imread('live.tif'
                                                    ))));
h=figure;
```

```
imagesc(im); colormap gray
hold on
size_cell_image=size(im); % Size of control image in pixels
quiver(X/pix,Y/pix,0
        *TFM.raw(k).dx_interp/pix,TFM.raw(k).dy_interp/pix);
axis image
xlabel('x [pixels]');
ylabel('y [pixels]');
title('Map of interpolated Y displacements')
axis([0 size_cell_image(2) 0 size_cell_image(1)]);
pause(0.1)
saveas(h,sprintf('interpolate_Y%d.tiff',k));
```

List of Figures

1.1 Schematic of an alveolus at the air-blood barrier. Squamous ATI cells provide the gas exchanging thin layer and cuboidal ATII cells secret surfactant through the release of lamellar bodies, reducing the surface tension at the air-blood barrier. Reused with permission from Nova et al. (2019) licensed under CC BY 4.0 https://creativecommons.org/licenses/by/4.0/. 3

1.2 Simplified structure of caveolae and their flattening with stretch. They are associated with stress fibers, a major regulator of membrane tension and cell shape. Reused with permission from Rausch & Hansen (2020) licensed under CC BY 4.0 https://creativecommons.org/licenses/by/4.0/. 4

1.3 Contractile forces exerted by cytoskeleton through focal adhesion on the underlying substrate. From "Cell traction force and measurement methods," by J. H-C. Wang and J-S Lin, 2007, Biomechanics and modeling in mechanobiology, 6, p. 361. Copyright 2007 by Springer Nature. Reprinted with permission. 5

1.4 (a) Spring model describing the Hooke's law, (b) Schematic of traction force microscopy. Traction forces are described as stresses $\sigma = F/A$ in Pa. Traction stress σ over the given area A results in displacement u on the surface which means the fluorescent markers near to the area will be displaced accordingly, at the same time the bottom of the film is considered to be fixed on a rigid base. By collecting the displacement of all the fluorescent markers one can compute the displacement field. . 6

2.1 Spin coating is a process that uses the centrifugal force to deposit a uniform thin film on flat substrates by rotating the substrate at high speeds. 10

2.2 Schematic of substrate variations for each experiment. (a) shows the main components prepared (b) on a glass cover slip attached to µ-Slide, and (c) on an elastic membrane. 11

2.3 Incubation of fluorescent beads on the membrane. 12

2.4 (a) Stretcher device, (b) pre-strain holders and clamps. 13

2.5 Perfusion set-up and pump system from ibidi. Image Source: Courtesy of ibidi GmbH. 16

2.6 ibidi pump controller software. ibidi GmbH. (2022). PumpControl Instruction Manual. Image Source: Courtesy of ibidi GmbH. 17

2.7 (a) and (b) fluorescent images taken from the beads before and after removal of the cell, (c) particle tracker decides which two beads are identical during the creation of displacement field (d) resulting in the stress field creation(e). 19

2.8 Graphical user interface for the poly-particle tracker by Rogers et al. (2007). The most important parameters are the radius, the file name that should be in the form of the address of the first image in the sequence, and the minimum track length that should be equal to the total number of images. 20

3.1 Bright field images of a 3T3 fibroblast cell on an un-stretched PDMS membrane made of Sylgard 184. All frames are showing the exact same spot on the membrane. Though the cell moved from position (a) to (b), no surface deformation was detected by the software (c). 21

3.2 Schematics of the previous and new membrane design. 22

3.3 Fluorescent images of beads distribution. (a) mixing the beads with diluted PDMS; aggregated beads and beads on different focal planes were not suitable for our TFM technique. (b) beads shrink with the solvent as it evaporates, and adhere together in big groups. (c) a nice distribution of fluorescent beads, ideal for TFM technique. 23

3.4 Wavy effect of n-Hexane the solvent of PDMS elastomer on polymerized PDMS and separation of the two PDMS layers. 23

3.5 Distribution of 0.5 µm beads at 5 µl (left) and 15 µl (right) per ml of buffer. 24

3.6 25

3.7 Defect growing in through the gel layer. 27

3.8 Partial visibility of the beads vs a precisely leveled membrane. 27

3.9 High cell density vs low cell density desired for TFM. 27

3.10 Fibroblast cells grown on a strip of fluerescent fibronectin coating. . . . 28

3.11 (a) Overview of the patterned area with hAELVi cells, (b) interpolated displacement, (c) traction before and (d) at 10% strain. 28

3.12 The overlap of the positions of beads detected in two fluorescent images of beads. Red spots show the position of beads in the control image, and blue spots indicate the beads in the cell image. (a) All beads seem to have moved due to the drift in images, and (b) shows the actual movement of beads after drift is removed with StackReg resulting in the creation of a displacement field (d). Marking the cell boundary (d) shows the detected displacement of beads to be relevant to cell location 30

3.13 Comparison between tracking results and displacement field created by (a) poly-particle tracker, (b) Mosaic particle tracker 2D/3D plugin, and (c) Blair/Dufresne tracker on a sample image. (d), (e), and (f) stress field calculations based on the displacement fields of (a), (b), and (c), respectively, emphasizing the importance of particle tracking quality when generating the stress field. (g) Tracking by PIV plugin on the same sample image. 32

3.14 Tracking of beads on a stretched membrane. Tracking only possible with frames taken every 0.5% strain giving a total of 21 frames for stretching from 0% to 10%. 33

3.15 Total traction forces of cells grown on plasma treated in comparison with the forces measured for cells on non-treated control substrate (n=8). . . 34

3.16 Total traction forces measure for hAELVi^{wt} (n=27), hAELVi$^{cav-/-}$ (n=24), and 3T3 fibroblast cells (n=15). 35

3.17 Total traction forces measurements for hAELVi^{wt} cells (a) without, (b) immediately after, and (c) 20 minutes after Blebbistatin treatment (n=5). 35

3.18 Stretch direction in relevance to image axis and force labeling. 36

3.19 Traction forces generated by hAELVi^{wt} cells per unit area. The box at 0% represents the forces in the unstretched phase before applying the strain. Plain boxes represent the forces during three stretch intervals to 50% while the shaded box represents the forces during a sudden increase of strain to 50%. Forces are shown in total amount, in the direction of the stretch and the transverse direction ($7 \leq n \leq 15$). 38

3.20 Stress relaxation of hAELVi^{wt} cells during 10 minutes of 50% static stretch. 39

3.21 Traction forces generated by hAELVi$^{cav-/-}$ cells per unit area. The box at 0% represents the forces in the unstretched phase before applying the strain. Plain boxes represent the forces during three stretch intervals to 50% while the shaded box represents the forces during a sudden increase of strain to 50%. Forces are shown in total amount, in the direction of the stretch and the transverse direction ($11 \leq n \leq 12$). 39

3.22 Cell area of hAELVi^{wt} and hAELVi$^{cav-/-}$ cells in the unstretched phase. 40

3.23 Partial detachment of a hAELVi$^{cav-/-}$ cell: (a) the unstretched phase, (b) under 50% strain, and (c) comparison of the cell boundary; the red dashes show where the cell was detached. 40

3.24 Percentage of cells of each type showing an increase or decrease in their areas. Most hAELVi^{wt} (WT) cells expanded with the stretch while most hAELVi$^{cav-/-}$ (KO) cells partially detached from the substrate. 41

3.25 Changes of the cell areas relative to the area of cells in the unstretched phase. 41

3.26 Strain energy density of empty membranes and membranes with a confluent layer of hAELVi^{wt} cells (n=6). 42

3.27 Strain energy [pJ] of a membrane stretched to 10% strain (red markers) in comparison to theoretical calculation. 42

3.28 Cell traction forces under shear stress during 10 minutes reducing constantly. Green arrow shows the flow direction. 43

3.29 Cell traction forces dropping under the shear stress within 10 minutes. 44

A.1 67

B.1 Structures **d** and **data**. If you manually transfer data to d, note that all four arrays must have the same n×2 dimension. 70

B.2 Cells inside the **TFM** structure containing different calculations such as displacement, stress, and surface energy density. Each cell is an n×n array with values referring to the same location on the live cell image with an n×n grid. 73

Declaration

I hereby declare that I have done the work for the present dissertation with the topic:
A Mechanobiosensor for Lung Cells
independently and have not used any other sources and resources than those indicated, have identified the passages taken over in words or content as references and have complied with the statutes of the University of Ulm for the Protection of Good Scientific Practice as currently published.
I agree that the dissertation may also be used for the purpose of verifying compliance with generally accepted scientific standards, in particular by using electronic data processing programs.

* Content was removed for data privacy protection reasons.